nature
cell biology

Myosin II controls cellular branching morphogenesis and migration in three dimensions by minimizing cell-surface curvature

Hunter Elliott[1,8,9], Robert S. Fischer[2,9,10], Kenneth A. Myers[2,3], Ravi A. Desai[4], Lin Gao[5,6], Christopher S. Chen[4,5,6], Robert S. Adelstein[7], Clare M. Waterman[2,9,10] and Gaudenz Danuser[1,9,10]

In many cases, cell function is intimately linked to cell shape control. We used endothelial cell branching morphogenesis as a model to understand the role of myosin II in shape control of invasive cells migrating in 3D collagen gels. We applied principles of differential geometry and mathematical morphology to 3D image sets to parameterize cell branch structure and local cell-surface curvature. We find that Rho/ROCK-stimulated myosin II contractility minimizes cell-scale branching by recognizing and minimizing local cell-surface curvature. Using microfabrication to constrain cell shape identifies a positive feedback mechanism in which low curvature stabilizes myosin II cortical association, where it acts to maintain minimal curvature. The feedback between regulation of myosin II by curvature and control of curvature by myosin II drives cycles of localized cortical myosin II assembly and disassembly. These cycles in turn mediate alternating phases of directionally biased branch initiation and retraction to guide 3D cell migration.

During migration in tissue *in vivo* or in culture in a three-dimensional (3D) extracellular matrix (ECM), endothelial cells, fibroblasts and tumour cells exhibit a characteristic complex shape that consists of a spindle-shaped cell body and arboreal, branched protrusions extending into the surrounding microenvironment[1–3]. This branched morphology is critical to invasion and path finding during angiogenesis, tissue repair and metastasis. Endothelial cell branching morphogenesis is mediated by regulation of the actomyosin cytoskeleton by both mechanical and biochemical cues[2,4–6]. Previous studies have shown that actin polymerization dynamics power plasma membrane protrusion to drive branch formation, which is counterbalanced by inhibition of branching through myosin II contractility[4,7]. Although much is known about the biophysical mechanism by which actin polymerization drives membrane protrusion to effect shape change[8], the basic principles by which myosin II contractility locally affects membrane geometry to inhibit cell branching and control global cell shape are unknown. Three central questions remain unresolved regarding the control of 3D cell shape by myosin II. The first concerns how the molecular-scale activity of myosin II motors is related to the cell-scale shape. Second, it is unclear whether cell shape in turn regulates actomyosin activity or assembly. Finally and most importantly, it remains to be determined how actomyosin is spatially and temporally controlled to mediate branching dynamics and guide invasive migration.

We used 4D imaging, computer vision and differential geometry to quantify cell shape and invasive migration of endothelial cells in 3D collagen ECMs. We found that myosin II motor activity regulates microscale cell-surface curvature to control cell-scale branch complexity and orientation. Myosin II preferentially assembles onto cortical regions of minimal surface curvature while also acting to minimize local curvature. Perturbations of Rho/ROCK signalling or myosin II ATPase function disrupt curvature minimization and branch regulation, but do not prevent curvature-dependent cortical assembly of myosin II. Myosin II contractility also controls branch orientation, possibly through differential association of myosin to outer low-curvature and inner high-curvature surfaces of branches, linking local

---

[1] Department of Cell Biology, Harvard Medical School, Boston, Massachusetts 02115, USA. [2] Cell Biology and Physiology Center, National Heart, Lung and Blood Institute, National Institutes of Health, Bethesda, Maryland 20892, USA. [3] Department of Biological Sciences, University of the Sciences, Philadelphia, Pennsylvania 19104, USA. [4] Department of Bioengineering, University of Pennsylvania, Philadelphia, Pennsylvania 19104, USA. [5] Department of Biomedical Engineering, Boston University, Boston, Massachusetts 02215, USA. [6] Wyss Institute for Biologically Inspired Engineering, Harvard University, Boston, Massachusetts 02115, USA. [7] Genetics and Developmental Biology Center, National Heart, Lung and Blood Institute, National Institutes of Health, Bethesda, Maryland 20892, USA. [8] Present address: Image and Data Analysis Core, Harvard Medical School, Boston, Massachusetts 02115, USA. [9] These authors contributed equally to this work.
[10] Correspondence should be addressed to R.S.F., C.M.W. or G.D.
(e-mail: fischerr2@nhlbi.nih.gov or watermancm@nhlbi.nih.gov or gaudenz.danuser@utsouthwestern.edu)

Received 12 February 2014; accepted 11 December 2014; published online 26 January 2015; DOI: 10.1038/ncb3092

curvature control to global directional control of migration. Thus, cell-surface curvature minimization is a core mechanism that translates the molecular activity of myosin II at the cortex into dynamic shape control for guiding invasive cell migration in three dimensions.

RESULTS

Cell-surface segmentation for defining quantifiable morphological parameters

To determine how myosin II controls cell shape and branching morphogenesis in a 3D microenvironment, we used primary aortic endothelial cells (AECs) embedded in collagen gels. This recapitulates key morphologic and dynamic features of endothelial tip cell migration during angiogenesis *in vivo*[4]. To visualize the shape of the cell surface, including thin cell protrusions, we used time-lapse 3D spinning disc confocal microscopy to image AECs derived from transgenic mice ubiquitously expressing tdTomato–CAAX to label the plasma membrane (Fig. 1a,b and Supplementary Fig. 1A and Video 1). We developed a robust methodology for the complete segmentation and numerical representation of the cell surface. To allow accurate segmentation of both dim, thin protrusions as well as the bright, thick cell body, we combined a 3D Gaussian partial-derivative kernel surface filtering algorithm with a self-adjusting high-intensity threshold that allowed the processing of variable image conditions without user intervention (Fig. 1c and Supplementary Methods and Fig. 1B–I). The resulting cell-surface representations were used for quantification of two types of feature that describe cell morphology during migration in three dimensions: the 'morphological skeleton' (Supplementary Video 2) to quantify cell-scale aspects of branching topology (Fig. 1d); and the local cell-surface curvature to quantify morphology nearer to the molecular length scale of actomyosin contractile units[9].

Myosin II activity inhibits dendritic branching

To investigate how myosin II activity regulates global branch organization, we derived from the morphological skeleton the number of branch tips and the branch complexity. Inhibition of myosin II ATPase activity with blebbistatin induced a complex cell morphology with an extensive network of thin branches (Fig. 1e,f), as noted previously[4]. As a measure of the branch complexity, we analysed the number of branch vertices along the path of each branch from the centre of the skeleton outwards (Fig. 1g). This showed that blebbistatin treatment promoted dendritic branching and increased branch path complexity (Fig. 1h,i), indicating that myosin II reduces cell branch number by minimizing the number of branch vertices. Furthermore, the dendritic nature of blebbistatin-treated cell morphology indicates that myosin II inhibition allowed branching to occur not only on the cell body, but at any point on the branch tree (Fig. 1e), suggesting that the regulation of branched cell shape occurs through myosin II acting locally at all points on the branched cell surface.

Myosin II suppresses branch tips and bases by minimizing local cell-surface curvature

To determine how myosin II controls cell shape locally, we mapped cell-surface curvature (Fig. 2a–c and Supplementary Methods and Fig. 2A–F) and determined the role of myosin II in its regulation. At each point on the cell surface, we determined the principal curvatures, κ_1 and κ_2, being the minimal and maximal values of curvature along two orthogonal axes, respectively, in the plane tangential to the surface. We specified a minimal curvature scale that excluded small surface fluctuations due to image noise and nanoscale processes such as endo- and exocytosis (Supplementary Methods and Fig. 2E,F). We verified the accuracy of our curvature measurements by imaging and analysis of fluorescent microspheres of known size embedded in collagen gels (Supplementary Fig. 2G–I), and excluded artefacts due to the microscope point-spread function geometry through simulations (Supplementary Methods and Fig. 2J–M).

Next, we categorized local surface curvature into four geometric classes relevant to cell shape features (Fig. 2a and Supplementary Fig. 3A–D and Supplementary Methods), and examined the role of myosin II in their regulation. These included hills (κ_1 and κ_2 are both positive), tubes (κ_1 is positive and κ_2 is close to zero), saddles (κ_1 is positive and κ_2 is negative) and invaginations (κ_1 and κ_2 are both negative). Mapping these classes onto cell-surface renderings showed that most of the cell body and branch surfaces were tube-like (Fig. 2b,d and Supplementary Video 3 and Fig. 3C,D), whereas hills localized primarily to branch tips, saddles localized to branch bases, and—although rare—invaginations localized to junctions of multiple branches oriented at acute angles to each other (Fig. 2B and Supplementary Fig. 3C,D). To determine how myosin II activity contributed to these shape features, we analysed AECs treated with blebbistatin. This showed that compared with the control, inhibition of myosin II increased the fraction of hills, invaginations and saddles, demonstrating that myosin II not only regulates overall branching, but also suppresses salient surface features such as branch tips and bases (Fig. 2b, bottom row and Supplementary Video 4 and Fig. 2d).

We then determined the role of myosin II in controlling the magnitude of cell-surface curvature. Curvature at any point on 3D surfaces can be described by either 'mean curvature' ($H=(\kappa_1+\kappa_2)/2$), 'Gaussian curvature' ($G=\kappa_1 * \kappa_2$), or 'maximal curvature' (maximum of $|\kappa_1|$, $|\kappa_2|$). Mapping mean curvature on control cells allowed visualization of the low mean curvature at branch bases, which increased as branches extended away from the cell body and their diameter decreased, and was highest at branch tips (Fig. 2c). Mapping mean curvature on blebbistatin-treated cells that exhibited extensive thin dendritic branches suggested that inhibition of myosin II increased curvature over the entire cell surface (Fig. 2c). To test this, we quantified the maximal, mean and Gaussian curvatures at all points on the surface of control and blebbistatin-treated cells and determined the per-cell median values. This showed that blebbistatin treatment significantly increased the median maximal and mean surface curvatures per cell (Fig. 2e). Gaussian curvature was also increased by myosin II inhibition, although not significantly because in both control and blebbistatin-treated cells, most surface points belong to the tube class, where κ_2 is $\sim$0 and hence the product $\kappa_1 * \kappa_2$ is insensitive to changes in the tube diameter, which are reflected in changes of κ_1. Together, this shows that myosin II activity minimizes local cell-surface curvature.

Our observations that myosin II inhibition affects both branch structure and surface curvature suggest that these global and local morphological parameters are interdependent. Qualitatively, this is not surprising, because the cell boundary describes a closed surface geometry. We tested this directly by correlating the median of the maximal curvature with the branch number on a per-cell basis, irrespective of treatment with blebbistatin (Fig. 2f). As the

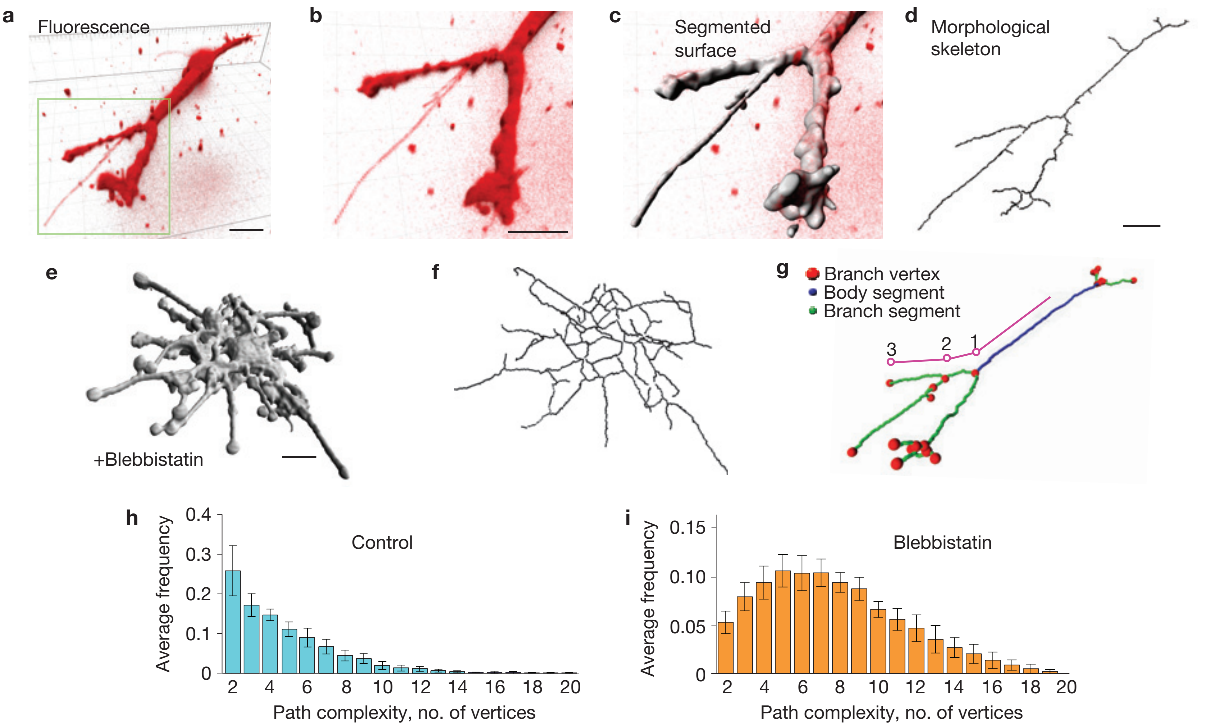

Figure 1 Quantification of cell morphological skeleton shows that myosin II limits branch complexity in three dimensions. (**a**,**b**) Living AEC in a 3D collagen gel expressing tdTomato–CAAX imaged by spinning disc confocal microscopy shown as a 3D shadow projection. Scale bars, 10 μm. (**b**) Rotated higher magnification of **a** to show thin branches. (**c**) Result of computational segmentation, with dim, thin protrusions accurately segmented. (**d**) Thinning of segmented volume to create a morphological skeleton. Scale bar, 10 μm. (**e**,**f**) Segmented surface (**e**) and morphological skeleton (**f**) of AEC treated with 20 μM blebbistatin to inhibit myosin II. Scale bar, 10 μm. (**g**) Parameterization of branch structure into a single main body segment (blue), branch segments (green) and vertices (red dots). Branch path complexity is calculated by following any path from a point on the skeleton at the body centre to a terminal branch segment and counting vertices along the path; one example path shown in pink. (**h**,**i**) Distribution of branch path complexity in control (**h**) and blebbistatin-treated (**i**) AECs. Data pooled from $n = 18$ cells for control, $n = 16$ cells for blebbistatin. Error bars show ±1.96 s.e.m. (approximate 95% confidence interval).

cell is largely tube-like, we focused on maximal curvature because it best represents the inverse of tube diameters. We found that within the natural variation of myosin II activation level in control cells as well as in myosin II-inhibited cells, branch number and surface curvature correlated over a wide range of values (Spearman's $\rho = 0.77$, $P < 1 \times 10^{-6}$), confirming that these two independently measured parameters are correlated. We conclude that our multiscale measurements are indeed interdependent.

Cell-surface curvature negatively regulates myosin II cortical localization

Our finding that myosin II regulates cell-surface curvature suggests that myosin II localization could be linked to curvature. Therefore, we determined whether myosin II cortical localization and local surface curvature were correlated in freely migrating cells. AECs from knock-in transgenic mice expressing GFP–myosin-IIA or GFP–myosin-IIB under endogenous promoters[4,10,11] were fixed in collagen gels and stained with Cell Tracker CM-DiI and fluorescent phalloidin to label the plasma membrane and F-actin, respectively (Supplementary Fig. 3F,H). We determined the local cortical myosin IIA and F-actin intensities and corresponding local surface curvature, carefully controlling for sampling artefacts (Supplementary Methods and Fig. 4A–L), and then categorized these surface curvatures. This showed that the highest myosin IIA concentration was associated with tube-like and saddle-shaped surfaces, with hills exhibiting very low myosin IIA (Fig. 3a). In contrast, F-actin exhibited a broad range of concentrations in tubes, saddles, and hills that are presumably the tips of actin-based protrusions (Fig. 3a and Supplementary Fig. 3E–H). Mapping cortical GFP–myosin-IIB intensity and local mean curvature on cell-surface renderings (Fig. 3c–f) confirmed these results for GFP–myosin-IIA.

To further analyse the distribution of cortical myosin IIA, IIB, and F-actin relative to surface curvature, we generated 2D histograms of mean curvature versus cortical intensity of GFP–myosin-IIA (Fig. 3g), GFP–myosin-IIB (Fig. 3h) and F-actin (Fig. 3i) over all surface points. This revealed a strong negative correlation between myosin IIA and mean curvature and a slightly weaker negative correlation between myosin IIB and mean curvature (myosin IIA, Spearman's $\rho = -0.50$, $P < 1 \times 10^{-6}$; myosin IIB, Spearman's $\rho = -0.32$ $P < 1 \times 10^{-6}$, Fig. 3g,h and Supplementary Fig. 4A–M and Supplementary Methods). In contrast, F-actin was associated with a broad range of mean surface curvatures, with a weak positive correlation (Spearman's $\rho = 0.17$ $P < 1 \times 10^{-6}$, Fig. 3i,j and Supplementary Fig. 3E–H). We conclude that myosin II localization in cells in three dimensions is not dominated by the total F-actin content at the cortex, but is specifically associated with cell-surface areas of lower curvature.

Our findings indicate that cortical myosin II concentration correlates with cell-surface curvature, suggesting that curvature could regulate myosin II localization. To test this directly, we externally enforced

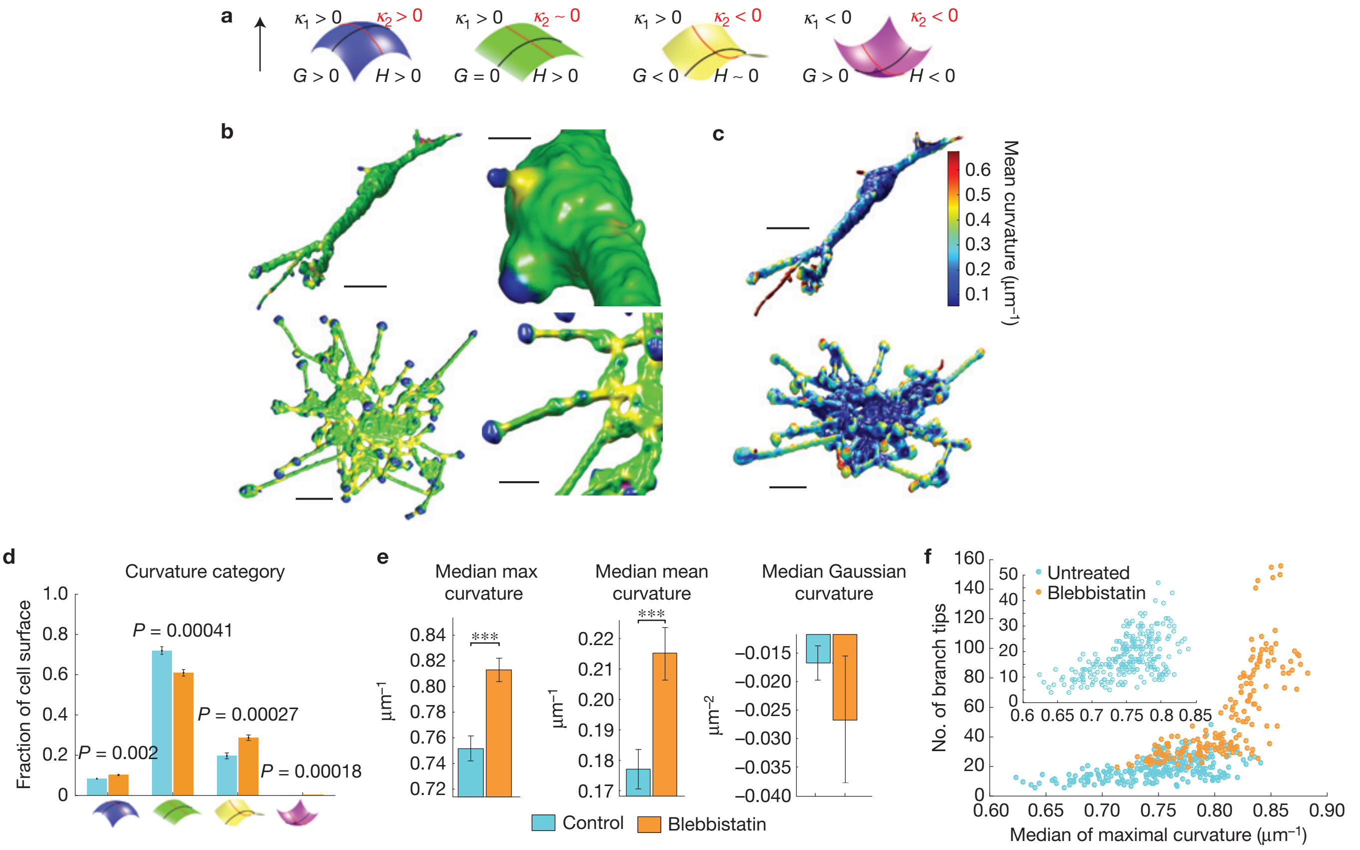

Figure 2 Myosin II regulates cell-surface curvature locally. (**a**) Schematic of the classification scheme for cell-surface curvature. Local curvature of a surface point is parameterized by two principal curvatures in orthogonal tangential directions, κ_1 and κ_2, where $\kappa_1 = 1/r_1$ (black lines) and $\kappa_2 = 1/r_2$ (red lines). Blue: a surface with both κ_1 and $\kappa_2 > 0$ resulting in a mean curvature, $H = (\kappa_1 + \kappa_2)/2 > 0$ and a Gaussian curvature $G = \kappa_1 * \kappa_2 > 0$, referred to as a hill. Green: cylindrical surface ($\kappa_1 > 0$ and $\kappa_2 \sim 0$), referred to as a tube. Yellow: κ_1 and κ_2 are of opposite signs, referred to as a saddle. Purple: concave surface with κ_1 and $\kappa_2 < 0$, referred to as an invagination. (**b**) Examples of different classes of surface curvature mapped onto cell surface using the colour scheme in **a**. Top row: control AEC; bottom row: blebbistatin-treated AEC. Scale bars, 10 μm on left, 3 μm in middle. (**c**) Mean curvature values mapped to cell surface of control (top) and blebbistatin-treated (bottom) cells from **b**. Mean curvature value scale bar shown on right. Scale bars, 10 μm. (**d**) Comparison of the fraction of the total cell surface in each of the surface curvature categories described in **a** for control cells (light blue, $n = 16$ cells) and cells treated with 20 μm blebbistatin (orange, $n = 16$ cells). Error bars show s.e.m., P values given above bars tested using Wilcoxon rank sum test. (**e**) Comparison of mean values of median maximal local curvature (maximum of $|\kappa_1|$, $|\kappa_2|$), absolute Gaussian curvature (G), and mean curvature (H) for multiple cells in control (light blue, $n = 16$ cells) or blebbistatin-treated (orange, $n = 16$ cells) conditions. Error bars show ±s.e.m., *** indicates $P < 0.01$ ($P = 5.37 \times 10^{-5}$ for max, $P = 1.38 \times 10^{-3}$ for mean and $P = 0.396$ for Gaussian curvature using Welch's two-tailed t-test). (**f**) Time-lapse imaging and analysis of the number of branches versus median maximum curvature for live AECs. Each point represents values for an individual cell at one time point. Control (blue, $n = 246$ time points, 14 cells) and myosin inhibition (orange, $n = 570$ time points, 27 cells) conditions. Inset shows data for control cells alone.

3D cell shape and analysed local cortical myosin II concentration with respect to surface curvature. Endothelial cells expressing GFP–myosin-IIA and tdTomato–CAAX were cultured in microfabricated agarose chambers assembled on the surface of collagen-coated coverslips (Fig. 4a,b). The walls of the chamber were non-adherent, yet constrained cells to a simple branched shape and imposed varied surface geometries (Fig. 4a). Cross-sections of branches showed that the lateral constraint imposed cylindrical geometries as the cell filled the chamber (Fig. 4c,c′). Registering multiple constrained cells in three dimensions allowed determination of the relationship between average imposed surface curvature (Fig. 4d) and average cortical GFP myosin IIA recruitment (Fig. 4f). We discounted the dorsal and ventral cell surfaces and limited our analysis to surfaces constrained by the non-adherent agarose walls. This showed that the CAAX plasma membrane marker localized relatively uniformly to the cell surface in a manner independent of local curvature (Fig. 4e). In contrast, GFP–myosin-IIA was absent from high-curvature branch tips, low along the unbranched rear of the cell body, but was enriched in areas of low mean curvature at the bases of branches and along their shafts (Fig. 4f). Plotting the ratio of normalized intensities of GFP–myosin-IIA or membrane label and the local mean curvature as a function of position along the confined cell edge confirmed this, and indicated a strong negative correlation between myosin IIA localization and curvature (Spearman's $\rho = -0.71$, $P < 1 \times 10^{-5}$; Fig. 4g and Supplementary Fig. 5A). Quantification of GFP–myosin-IIA intensity versus mean curvature for all points on the confined surfaces of multiple cells showed a similar inverse correlation (Spearman's $\rho = -0.23$, $P < 1 \times 10^{-6}$, Fig. 4h) as was observed for cells migrating freely in 3D collagen ECMs, suggesting that low mean curvature is sufficient to recruit myosin IIA. In contrast, the membrane label showed no

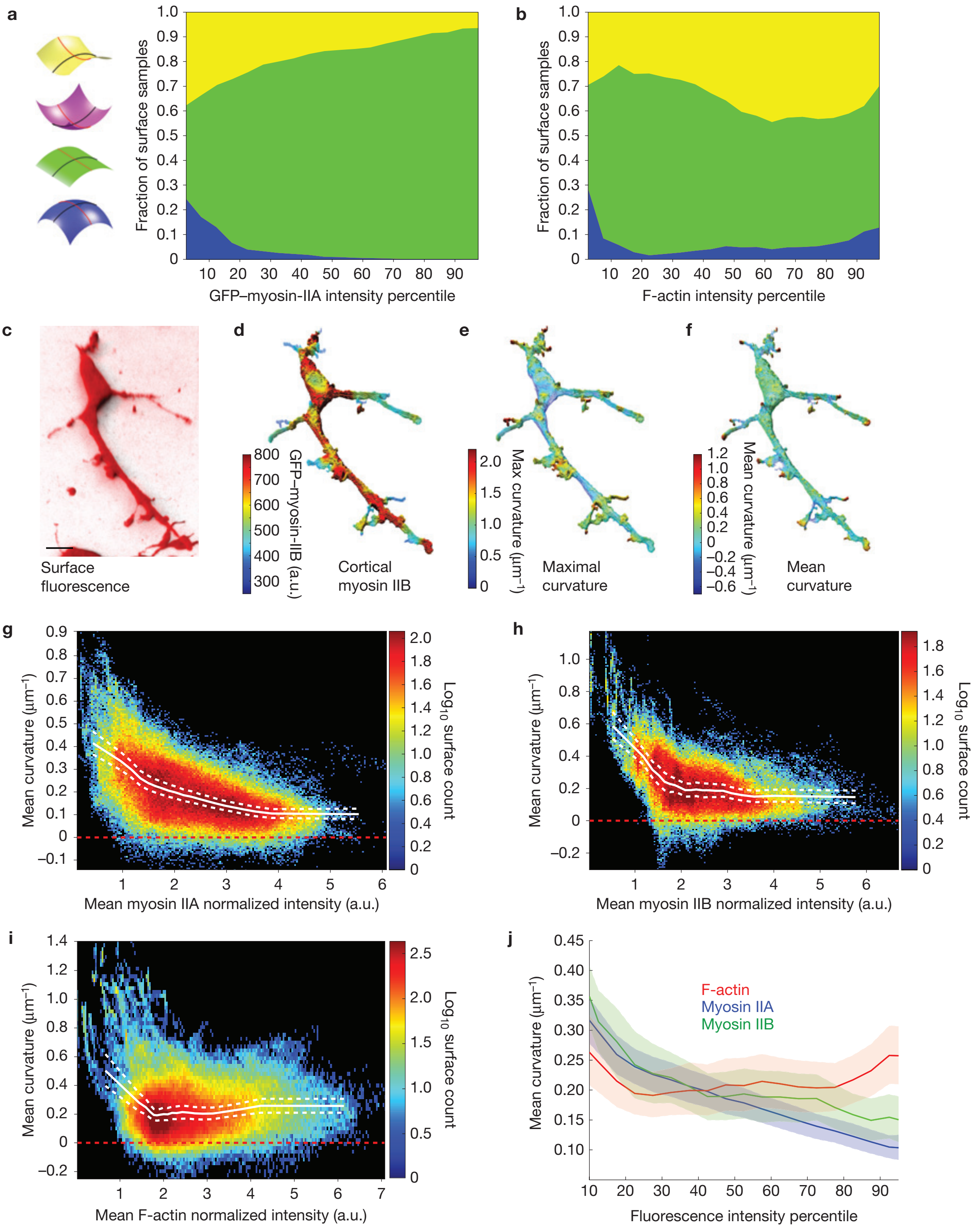

Figure 3 Cortical myosin II associates with minimal surface curvature. (**a**,**b**) Fraction of the population of surface points of a given cortical mean myosin-II–GFP (**a**) or F-actin (**b**) intensity, whose curvature is categorized according to the colour scheme shown ($n = 268{,}844$ points on 25 cells for **a**, $n = 230{,}475$ points on 25 cells for **b**). Note that there were a negligible number of points in the 'invagination' category. (**c**–**f**) AEC in 3D collagen gel expressing tdTomato–CAAX and myosin-IIB–GFP. Scale bar, 10 μm. (**c**) 3D shadow projection of tdTomato–CAAX fluorescence. (**d**–**f**) Colour-encoded (highest: red, lowest: blue) normalized values of mean cortical myosin-IIB–GFP intensity (**d**); local absolute maximum curvature (**e**); and local mean curvature (**f**); mapped onto the segmented cell surface. (**g**–**i**) Distributions of mean cortical GFP–myosin-IIA, GFP–myosin-IIB, or phalloidin-stained F-actin intensity as a function of mean surface curvature for all surface points ($n = 268{,}844$ points from 15 cells for **g**; $n = 167{,}449$ points from 14 cells for **h**, and $n = 230{,}475$ points from 15 cells for **i**). Colour scale indicates $\log_{10}$ of number of surface point samples; solid white line, mean curvature value for each intensity value; dashed line, bootstrapped 95% confidence intervals of the mean. (**j**) Mean curvature plotted versus mean intensity as a percentile rank for cortical F-actin, myosin IIA and myosin IIB, as for solid lines in **g**–**i**. Faded colour background areas indicate the 95% confidence limits by subsampled bootstrap for each curve (Supplementary Methods).

correlation between intensity and curvature (Spearman's $\rho = -0.093$, $P = 8.8 \times 10^{-164}$, Supplementary Fig. 5B). In summary, myosin II is recruited to minimally curved cortical surfaces in freely migrating cells, and by imposing cell shape externally, we show that local cell-surface curvature negatively regulates myosin II localization to the cortex. Together with the finding that disruption of myosin II activity increased cell-surface curvature, these results suggest a positive feedback loop in which myosin II minimizes local curvature to promote its recruitment to the cortex, thus maintaining low cell-surface curvature.

Myosin II assembly at the cortex in response to low curvature is independent of contractility

We then sought to determine how cell-surface curvature negatively regulates myosin II localization. We considered three possible mechanisms by which curvature could control local assembly of cortical myosin II: curvature-dependent upstream signalling; tension-dependent regulation of myosin II assembly; or curvature-dependent stabilization of cortical binding. To test whether myosin II was regulated by signalling to control its local assembly/activation, we first determined whether myosin II phosphorylation was spatially regulated. We immunolocalized myosin II regulatory light chain phosphorylated on Ser 19 (pS19-MRLC) in cells expressing GFP–myosin-IIA (refs 12,13). Co-localization analysis in three dimensions revealed no substantial difference in localization of the two markers, suggesting that differences in myosin IIA localization or its association with curvature could not be accounted for by local regulation of phosphorylation (Supplementary Fig. 6C). We perturbed signalling upstream of pS19-MRLC and determined the effects on curvature-dependent localization of myosin II. We inhibited either ROCK, which directly phosphorylates S19-MRLC (ref. 14), with Y-27623 (Fig. 5a), or its upstream activator, Rho, with exoenzyme C3 (Fig. 5b) in cells expressing GFP–myosin-IIA. Like blebbistatin, these agents increased cell branching and branch path complexity (Supplementary Fig. 6A), suggesting that activation of myosin II through Rho/ROCK signalling regulates branching. In spite of their effects on cell shape changes, these inhibitors had no effect on the inverse correlation between cortical myosin IIA localization and local mean surface curvature, although, as expected, the curvature distribution was shifted to higher values (Fig. 5d,e) compared with the control. Similar results were found for analysis of cells expressing GFP–myosin-IIB, where treatment with Y-27623 or ML-7 (that blocks myosin light chain kinase) increased cell branching and curvature, but preserved the negative correlation between cortical GFP–myosin-IIB intensity and mean curvature (Supplementary Fig. 6B). None of the treatments altered the relationship between actin localization and curvature (Fig. 5h). Thus, myosin II assembles at the cortex in a curvature-dependent manner, independent of signals that control regulatory light chain phosphorylation. This suggests that local signalling and activation of myosin II, although required for cell shape regulation, is not responsible for localized myosin II assembly at the cortex.

As tension in a surface also decreases curvature, we tested whether actomyosin-mediated cortical tension regulated the curvature-dependence of myosin II localization. We inhibited motor activity either pharmacologically or with a mutation in myosin IIA heavy chain, R702C, which reduces ATPase activity and causes haematologic and kidney defects in humans and mice[15,16]. Analysis of the curvature-dependence of GFP–myosin-IIA or GFP–myosin-IIB cortical localization in AECs treated with blebbistatin (Fig. 5c) showed that even in the presence of blebbistatin, local myosin II intensity inversely correlated with mean curvature (Fig. 5f and Supplementary Fig. 6B). We performed similar analysis on AECs derived from mice heterozygous for GFP–R207C-myosin-IIA. Examination of AECs in three dimensions suggested that this mutant induced a slight elevation in cell branching (Fig. 5g). However, analysis of localization relative to mean curvature demonstrated that GFP–myosin-IIA-R702C was still localized to the cortex with curvature-dependence (Fig. 5j). Again, these perturbations did not affect the curvature-independence of cortical F-actin (Fig. 5h). Thus, our data show that motor activity is not required for the curvature-dependent localization of myosin II, suggesting that the association of myosin II with low-curvature cortical surfaces is independent of actomyosin-mediated cortical tension.

We then sought to determine whether curvature regulated the stability of cortical binding by myosin II. We analysed the relationship between curvature and the stability of GFP–myosin-IIA association with the cortex by fluorescence recovery after photobleaching. We measured the fraction of fluorescence recovery in a bleached region on the cortex and compared this value in branches of large (low maximal curvature, $d > 5\,\mu\text{m}$) and small (higher maximal curvature, $d < 4\,\mu\text{m}$) diameter. This showed that a larger fraction of GFP–myosin-IIA was stably associated with the cortex (less recovery of fluorescence) in low- compared with high-curvature branches (Fig. 5i, $P < 0.001$). Hence, myosin IIA association with the cortex is stabilized by lower curvature.

The perturbation experiments above provide insight into the mechanism of cortex binding by myosin II. Blebbistatin blocks myosin II ATPase activity by locking myosin II in a weakly bound state[15]. Although blebbistatin did not affect the inverse correlation between myosin II localization and curvature (Fig. 5f), analysis of F-actin and myosin IIA co-localization showed that myosin IIA was only partially displaced from cortical F-actin by blebbistatin (Fig. 5k,l). This suggests that actin binding is critical to cortical association of myosin II. Together, these data show that curvature regulates the localization of myosin II at the cortex not by local control of signalling or contractility, but by stabilizing the association of myosin II with low-curvature regions of the cortex, possibly mediated by F-actin binding.

3D cell migration is mediated by branching/debranching cycles that are driven by cycles of myosin II cortical dissociation/association

Our results show that myosin II regulates and responds to cell-surface curvature. To approach how this mediates dynamic control of cell shape during migration in three dimensions, we analysed the temporal relationships between parameters of cell movement, branching, cell-surface curvature and myosin II recruitment to the cortex. We determined the morphological skeleton and local surface curvature over time in AECs expressing tdTomato–CAAX during migration in 3D collagen (Fig. 6a and Supplementary Video 5). Tracking of the cell centre (Supplementary Fig. 6D–F and Video 6) showed that cells moved in a pulsatile manner, speeding up and slowing down at varying intervals (Fig. 6b). Autocorrelation analysis demonstrated that cell speed fluctuations were not due to positional noise, but represented stochastic pulses in cell instantaneous velocity (Supplementary Fig. 6G). Analysis of cell centre movement relative to the evolution of the morphological

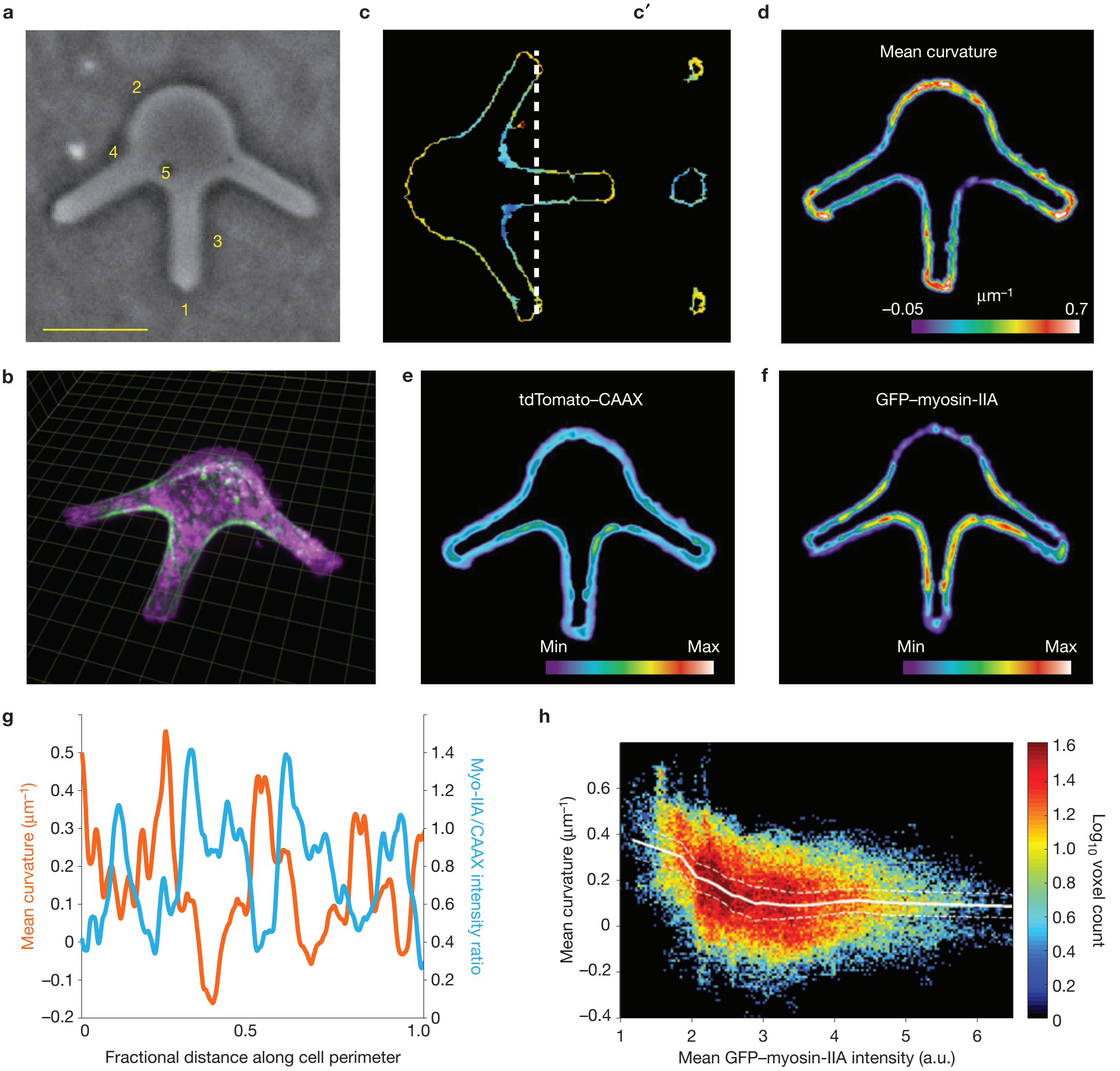

Figure 4 Externally imposed local curvature modulates myosin IIA localization to the cortex. Human umbilical vein endothelial cells expressing tdTomato–CAAX and myosin-IIA–GFP were plated into microfabricated agarose chambers to constrain their 3D shape. (**a**) Phase-contrast image of 30-µm-deep agarose chambers, the vertical walls of which enforce five regimes of decreasing mean curvature: high positive mean curvature at tips (1) to lowest mean curvature at saddle-like structures (5). Scale bar, 20 µm, applies to **a**,**c**–**e**. (**b**) Cells expressing GFP–myosin-IIA (green) and tdTomato–CAAX (purple) were subjected to 3D spinning disc confocal microscopy, and maximal intensity projection of a 3D stack (with rotation) is shown; grid spacing is 5 µm. (**c**) *XY* cross-section of an example cell with segmented local mean surface curvature calculated from cell-surface renderings of tdTomato–CAAX and displayed according to the heat map shown in **d**. (**c′**) *YZ* cross-section at position indicated by dashed line in **c**. (**d**–**f**) Averaged measurements at constrained surfaces of multiple cells ($n=6$). (**d**) Mean curvature (colour scale in μm^{-1}; length of colour bar is 40 µm). (**e**) tdTomato–CAAX intensity. (**f**) GFP–myosin-IIA intensity. In **e** and **f**; colour scales for both are in arbitrary units. (**g**) Averaged GFP–myosin-IIA/tdTomato–CAAX intensity ratio (blue), and mean curvature (red) as a function of position along the perimeter of an agarose chamber ($n=6$ cells). (**h**) Mean cortical GFP–myosin-IIA intensity as a function of mean surface curvature for all confined surface points of multiple cells in individual chambers. Colour scale indicates $\log_{10}$ of number of surface point samples, $n=95{,}126$ surface points sampled from 6 cells. Solid white line is mean curvature for each intensity bin; dashed white lines show bootstrapped 95% confidence interval of mean.

skeleton in three dimensions over time showed that branch number and cell centre velocity seemed out of synch (Fig. 6b). Indeed, temporal cross-correlation between total branch radius (branch number weighted by branch radius) and cell centre velocity indicated significant negative correlations at all negative time lags, but a strong positive correlation peak at a positive time lag of ~1,200 s. This indicates that branch number increases during periods of low cell velocity, and branch pruning precedes rapid cell body advance by ~20 min (Fig. 6c). Similarly, total branch complexity (sum of all branch vertices per time point) also fluctuated out of synch with cell centre velocity (Fig. 6d). However, in this case, the temporal cross-correlation exhibited a peak of negative correlation at zero time shift, indicating

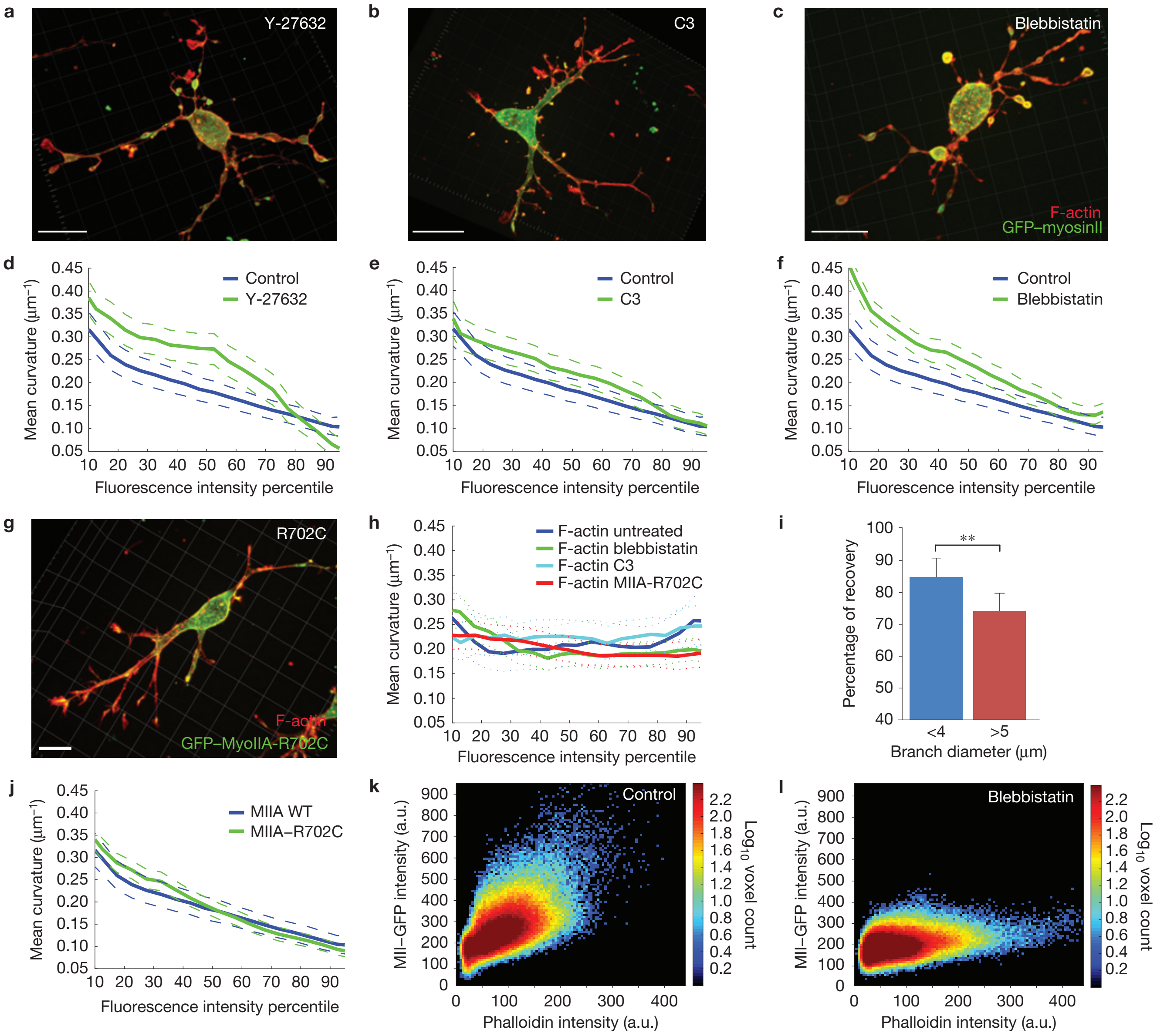

Figure 5 Curvature-dependent myosin II association with the cell cortex is independent of myosin II motor activity. (**a**–**c**) AECs expressing GFP–myosin-IIA (green) in a 3D collagen gel exposed to 2 mM Y-27632 (**a**), 100 μg ml^{-1} C3-exoenzyme (**b**), or 20 μM blebbistatin (**c**) were fixed and stained with fluorescent phalloidin (red). Maximal intensity projections of 3D reconstruction are shown. (**d**–**f**) Mean curvature plotted versus mean intensity as a percentile rank for cortical myosin IIA in the presence (green) or absence (blue) of inhibitors indicated. Control data are re-plotted on each graph for comparison. Solid lines show mean curvature value for each intensity value; dashed lines show bootstrapped 95% confidence about the mean. $n=7$ cells, 268,844 points for control; $n=7$ cells, 393,282 points for Y-27632; $n=7$ cells, 379,475 points for C3; and $n=15$ cells, 968,398 points for blebbistatin. (**g**) An AEC expressing GFP–myosin-IIA-R702C (green) in a 3D collagen gel was fixed and stained with fluorescent phalloidin (red). Maximal intensity projection of 3D reconstruction is shown. (**h**) Mean curvature plotted versus cortical F-actin mean intensity as a percentile rank for all conditions in **a**–**g**,**j**. (**i**) AECs in a 3D collagen gel expressing myosin-IIA–GFP were subjected to localized fluorescence photobleaching and recovery and imaged by 3D spinning disc confocal microscopy. Percentage of fluorescence recovery at the cortex in small- ($<$4 μm) and large- ($>$5 μm) diameter branches ($n=18$ for small branches, $n=18$ for large branches, error bars show standard deviation, $P<0.001$ using Students two-tailed *t*-test) is shown. (**j**) Mean curvature plotted versus mean intensity as a percentile rank for wild-type GFP–myosin-IIA (blue) or GFP–myosin-IIA-R702C (green). $n=19$ cells, 797,766 points for R702C. Note wild-type data are reproduced from **c** control data for comparison. Scale bars in micrographs equal 10 μm. (**k**,**l**) Direct comparison of local cortical F-actin and myosin IIB in the presence (**l**) and absence (**m**) of blebbistatin shown in 2D per-voxel distributions. Although the ratio (slope) of myosin II to F-actin is lowered by blebbistatin, much of the myosin II remains associated with F-actin at the cortex.

that dendritic branching impedes cell movement (Fig. 6e). In support of this, for individual cells, the mean total branch complexity over time was inversely correlated with mean speed over time (Fig. 6f). Thus, AECs migrate in a 3D microenvironment by alternating between phases of dendritic branch expansion, which inhibits cell movement, followed by debranching to allow cell body advance.

As cell branching and cell-surface curvature are linked (Fig. 2f), the above result predicts that curvature would fluctuate similarly to

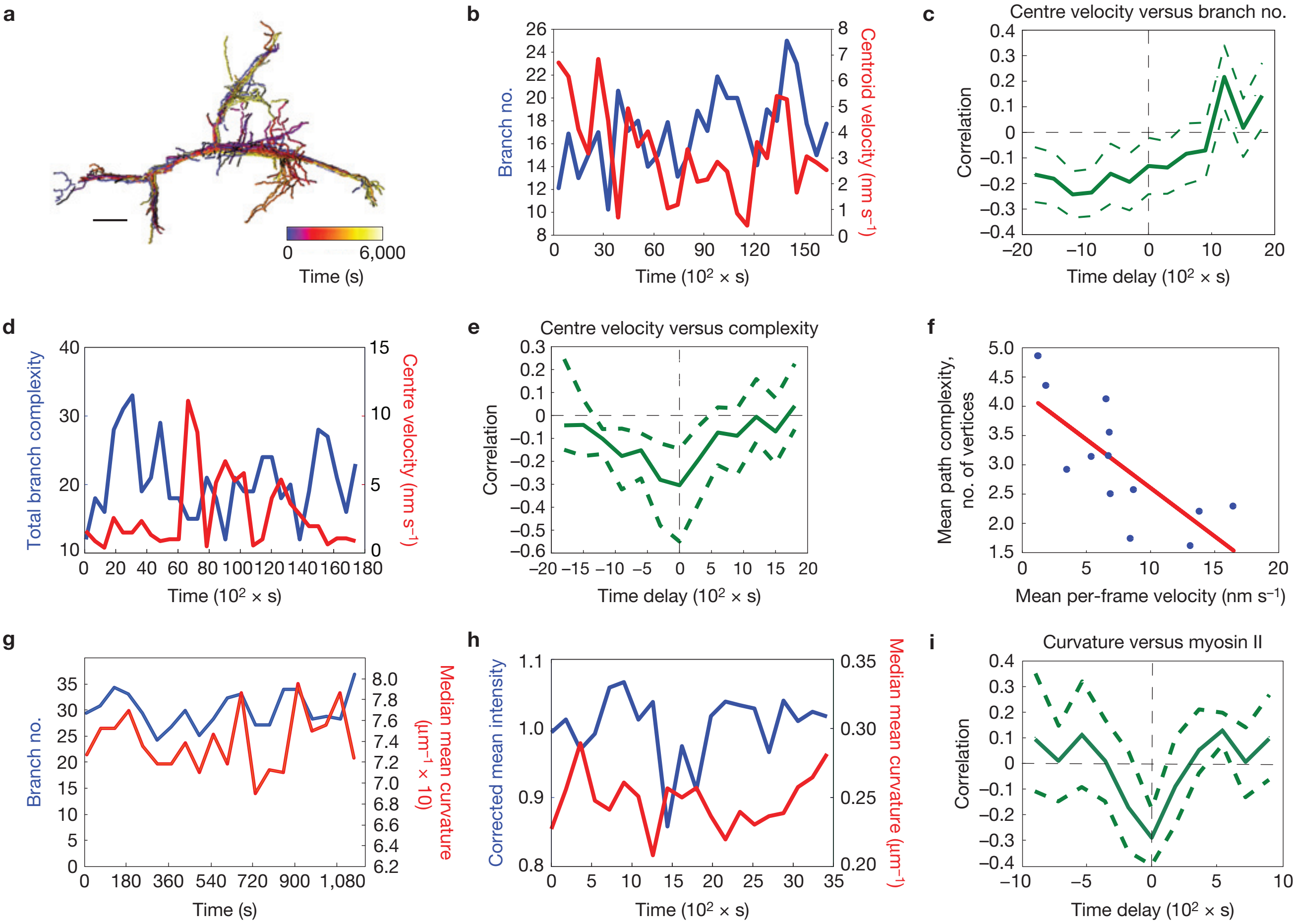

Figure 6 Myosin II dynamically associates with the cortex to control cycles of AEC branching and movement by local minimization of surface curvature to guide cell migration. Living AECs migrating in a 3D collagen gel expressing tdTomato–CAAX (and myosin-IIA–GFP where indicated) were imaged by time-lapse 3D spinning disc confocal microscopy. (**a**) Evolution of 3D morphological skeleton, colour encoded according to elapsed time (scale bar, 10 μm). (**b**) Time courses of branch number (number of branch tips, blue) and instantaneous cell centroid velocity (red) for a representative AEC. (**c**) Temporal cross-correlation analysis of branch number versus cell centre velocity (data pooled from $n=8$ cells, >180 min each). Positive delay indicates that change in branch number precedes change in velocity. (**d**) Time courses of cell branching complexity (total number of branch vertices, blue) and centroid velocity (red) for a representative migrating AEC. (**e**) Temporal cross-correlation analysis of cell branching complexity versus centroid velocity (data pooled from $n=8$ cells, >180 min each). Positive delay indicates that change in velocity precedes change in cell branching complexity. (**f**) Mean cell branching complexity versus mean velocity for individual AECs (blue circles, means determined from 100 min time-series per cell). Red line, best linear fit; slope = −0.21 vertices $\text{nm}^{-1}\,\text{s}^{-1}$, slope 95% confidence interval −0.32 to −0.11. (**g**) Time courses of branch number (number of branch tips, blue) and median mean curvature (red) for a representative AEC. (**h**) Plot of photobleach-corrected mean intensity of myosin-IIA–GFP at the cortex (blue) versus the median mean curvature (red) of a region of a branching AEC over time. (**i**) Temporal cross-correlation analysis of local mean cortical myosin-IIA–GFP intensity versus local mean curvature (data pooled from $n=11$ regions from 10 cells, 20 time points each). Positive delay indicates that curvature change follows myosin II change. In **c**,**e** and **i**: solid line, correlation; dashed lines, 95% confidence interval determined by 1,000 bootstrap estimations of correlation functions (see Supplementary Methods).

branching during migration. In individual cells, as branch number varied over time, the median mean surface curvature varied in synch (Fig. 6g). As myosin II localization and curvature are inversely correlated (Figs 3 and 4), this further predicts that myosin II association with the cortex would fluctuate out-of-phase with curvature during migration. Time-lapse 3D imaging (60 s intervals) of GFP–myosin-IIA and tdTomato–CAAX in AECs migrating in 3D collagen gels and analysis of mean surface curvature and cortical GFP–myosin-IIA intensity showed that mean cortical GFP–myosin-IIA intensity and median mean curvature both fluctuated over time (Fig. 6h and Supplementary Video 7). Temporal cross-correlation between myosin IIA intensity and median mean curvature within dynamically active regions of the cell cortex (Supplementary Video 8) exhibited a significant negative correlation at zero time lag, indicating that cortical myosin IIA concentration increased and curvature decreased in synchrony (Fig. 6i). Hence, during cell migration, cycles of exploratory branching followed by debranching and subsequent cell body advance are associated with cycles of myosin II dissociation from the cortex that allow plasma membrane curvature, followed by myosin II cortical recruitment that promotes curvature minimization.

Myosin II controls branch orientation to mediate directional cell movement in three dimensions

In addition to regulating cell branching, myosin II activity also promotes directional persistence of migration in three dimensions[4,7]. Therefore, we analysed the role of myosin II in controlling branch

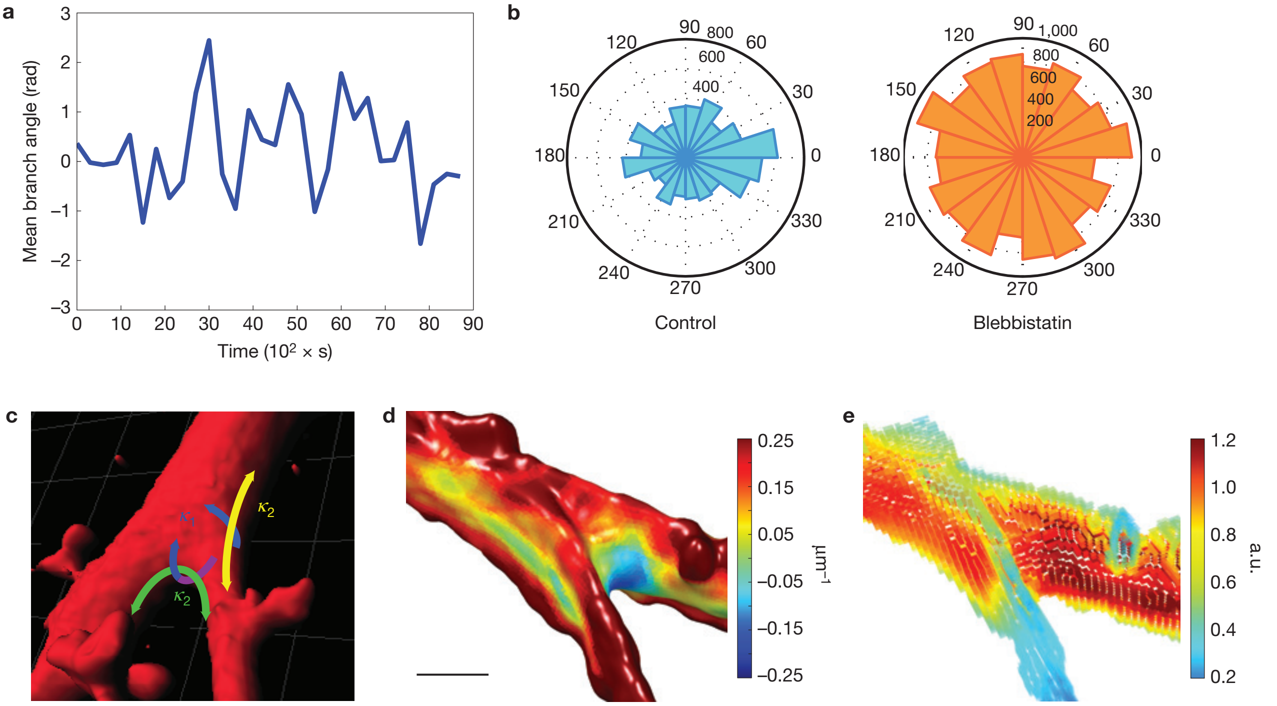

Figure 7 Myosin II biases branch orientation in the direction of migration and shows differential association with inner high-curvature and outer low-curvature saddles at a branch base. (**a**) Quantification of branch angle over time. An example cell was imaged every 300 s over time, and for each time point, a morphological skeleton was extracted as described in the Supplementary Methods. All branch vectors for a given time point were summed to derive a mean branch angle relative to the migration direction over all time points. (**b**) Radial histograms of branch angle relative to the direction of cell migration in the presence or absence of $20\,\mu$M blebbistatin; total branches indicated as radii shown for each condition over $n=13$ cells, 286 time points for control; $n=11$ cells, 129 time points for blebbistatin. (**c**) A typical branch geometry shown in a surface rendering of a branch region in AECs, with two sets of principle curvatures, one parallel to a plane containing the branch angle (κ_2, green and yellow) and one perpendicular (κ_1, blue). The out-of-plane curvatures of the two saddles are comparable to each other and are dominated by the radii of the branches, whereas the in-plane curvatures differ significantly with the saddle at the inner surface forming a higher negative curvature than the saddle at the outer surface. (**d**) Example of acute branch junction, where a long region of low maximal curvature occurs at the outside of the branch in the plane of the branch angle; a much smaller region of low maximal curvature occurs inside the branch junction. Colour scale indicates local maximal curvature. (**e**) Heat map of GFP–myosin-IIA at the cortex in the same branch junction. Colour scale map indicates arbitrary units of GFP–myosin-IIA.

directionality in AECs expressing tdTomato–CAAX during migration in 3D collagen. From the morphological skeleton, we determined branch angle relative to the direction of cell centre movement. Plotting mean branch angle over time showed that, similar to branch number (Fig. 6b) and branch complexity (Fig. 6d), mean branch angle also fluctuated over time (Fig. 7a). Rose plots of mean branch angle relative to the direction of cell movement showed that branches with near-normal angles relative to the cell axis were rare, indicating that branch angle was biased along the axis of cell movement (Fig. 7b). Treatment of cells with blebbistatin removed this bias, and fully randomized branch angle (Fig. 7b). Together, our results indicate that cells migrate by cyclically varying branch angle relative to the direction of cell movement, and maintain directionality by myosin II-mediated minimization of branch angle.

We then sought to understand how myosin II might control branch angle through local curvature sensing and regulation. In general, branches oriented normal to the cell body have similar curvature all around their bases, whereas branches oriented at non-normal angles relative to the cell body consist of two opposing saddle structures: one associated with the acute angle at the inner surface and one associated with the obtuse angle at the outer surface, creating potential for curvature asymmetry (Fig. 7c). Accordingly, asymmetric accumulation of myosin II at these sites could enhance overall minimization of curvature in the branch junction, favouring acute angles (Fig. 7b,e). On the other hand, myosin II accumulation at the bases of branches normal to the cell body would be equal in all directions, allowing retraction of the branch to minimize curvature. Inspection of time-lapse videos of GFP–myosin-IIA dynamics confirmed an even recruitment of myosin IIA to the saddles all around the base of normal angles (Supplementary Video 9). We observed in time-lapse videos that rare normal branches were rapidly retracted, whereas slanted branches with asymmetric myosin accumulation tended to be more stable. Although this mechanism will require further investigation to characterize quantitatively, our observed examples suggest that myosin II could bias branch direction by asymmetric association with and curvature minimization of acute branches and/or retraction of normal branches to minimize overall branch angle relative to the cell body, thus favouring branch formation along the direction of movement.

DISCUSSION

Our development of an image analysis framework for quantifying 3D cell morphology across length scales has revealed how myosin II acts at the molecular scale to minimize local cell-surface curvature, which in turn regulates the interlinked parameter of cell-scale branching morphogenesis. Combining this analysis with microfabrication to constrain cell shape identifies a positive feedback mechanism in which cell shape regulates myosin II, such that the motor preferentially binds to and is stabilized by lower-curvature cortical regions, where it acts to maintain minimal curvature. This feedback loop of local myosin II regulation by and activity on curvature mediates cycles of spatially controlled cortical myosin II assembly and disassembly that correlate with cycles of branch initiation and retraction to guide 3D cell migration.

How might myosin II motors regulate and respond to surface curvature? We suggest that myosin II minimizes cell-surface curvature through generation of motor-driven tension in an isotropic cortical actin network attached to the plasma membrane, similar to how surface tension drives membrane flattening to minimize curvature in soap bubbles or membrane-bounded organelles[17]. The question of how myosin II responds to curvature, however, is more complex. Our analysis suggests that curvature-dependent recruitment of myosin II to the cortex is independent of Rho/ROCK signalling or contractile activity, but that curvature stabilizes its binding to cortical actin. We speculate that because non-muscle myosin II mini-filaments exist as linear 300-nm rods with bouquets of actin-binding heads at each end[18], a maximal number of heads would engage an actin network that extends in the plane of the rod (Supplementary Fig. 7). Extrapolating this concept suggests that high tube-like curvature would favour maximal head engagement for rods aligned along the zero-curvature axis, thus orienting contractile forces along the branch axis, providing a mechanism for retracting thin branches or generating traction on ECM-adhered branch tips. Alternatively, because curvature and tension in a closed surface at equilibrium are inextricably linked by the Young–Laplace relation, myosin II recruitment to the cortex could be regulated by tension[19]. However, our manipulations of motor activity demonstrate that curvature-sensitivity of myosin II recruitment is independent of actomyosin tension. One possible reconciliation of our proposed geometric versus tension-dependent models is that tension-dependent changes in actin organization could alter the optimal myosin II head engagement to enhance myosin II recruitment without requiring myosin contractility directly.

Our observations support a model in which curvature-sensitive recruitment and turnover of myosin II defines the central switch in a directionally biased branching–debranching cycle that drives directed cell migration in complex 3D environments. The cycle is initiated by local fluctuations in cortical myosin II concentration. Local concentration depressions allow F-actin polymerization and/or hydrostatic pressure to overcome cortical tension and push out protrusions, which are stabilized by adhesion to the ECM (ref. 20). Thin branches with high curvature initially survive because of low myosin II recruitment and thus low contractility, whereas more mature branches with lower curvature must maintain stronger polymerization and/or adhesion forces to overcome increasing contraction driven by recruitment of myosin II to their low-curvature cortex. Thick branches that are not stabilized by adhesion are retracted if they are normal to the cell surface by even accumulation of myosin II around their bases and aligned along their length (Supplementary Video 9). The migration cycle ends when large-scale axial contraction of the low-curvature cell body cortex overcomes the anchoring forces of the adhesion-stabilized branches that are aligned with guidance cues. Thus, curvature-sensitive myosin II recruitment may provide a robust core mechanism for cell shape control and branch morphogenesis in cell migration across a range of length scales from the local initiation of a branch to global traction generation at the cell scale. ◻

METHODS

Methods and any associated references are available in the online version of the paper.

Note: Supplementary Information is available in the online version of the paper

ACKNOWLEDGEMENTS

This work was initiated as a collaborative effort between R.S.F. and G.D. (NIH R21 CA124990). H.E. and G.D. are supported by NIH R01 GM090317. R.S.F., R.S.A., K.A.M. and C.M.W. are supported by the NHLBI Division of Intramural Research.

AUTHOR CONTRIBUTIONS

H.E., R.S.F., C.M.W. and G.D. designed experiments and wrote the manuscript. R.S.F. performed all imaging and FRAP experiments. H.E. designed, implemented and applied analysis software. R.S.A. provided transgenic mice. R.S.F., K.A.M., R.A.D., L.G. and C.S.C. performed microfabricated coffin experiments.

COMPETING FINANCIAL INTERESTS

The authors declare no competing financial interests.

1. Doyle, A. D., Petrie, R. J., Kutys, M. L. & Yamada, K. M. Dimensions in cell migration. *Curr. Opin. Cell Biol.* **25,** 642–649 (2013).
2. Grinnell, F. Fibroblast biology in three-dimensional collagen matrices. *Trends Cell Biol.* **13,** 264–269 (2003).
3. Baker, B. M. & Chen, C. S. Deconstructing the third dimension: how 3D culture microenvironments alter cellular cues. *J. Cell Sci.* **125,** 3015–3024 (2012).
4. Fischer, R. S., Gardel, M., Ma, X., Adelstein, R. S. & Waterman, C. M. Local cortical tension by myosin II guides 3D endothelial cell branching. *Curr. Biol.* **19,** 260–265 (2009).
5. Hung, R. J. *et al.* Mical links semaphorins to F-actin disassembly. *Nature* **463,** 823–827 (2010).
6. Petrie, R. J., Doyle, A. D. & Yamada, K. M. Random versus directionally persistent cell migration. *Nat. Rev. Mol. Cell Biol.* **10,** 538–549 (2009).
7. Petrie, R. J. & Yamada, K. M. At the leading edge of three-dimensional cell migration. *J. Cell Sci.* **125,** 5917–5926 (2012).
8. Krause, M. & Gautreau, A. Steering cell migration: lamellipodium dynamics and the regulation of directional persistence. *Nat. Rev. Mol. Cell Biol.* **15,** 577–590 (2014).
9. Lecuit, T., Lenne, P. F. & Munro, E. Force generation, transmission, and integration during cell and tissue morphogenesis. *Annu. Rev. Cell Dev. Biol.* **27,** 157–184 (2011).
10. Bao, J., Ma, X., Liu, C. & Adelstein, R. S. Replacement of nonmuscle myosin II-B with II-A rescues brain but not cardiac defects in mice. *J. Biol. Chem.* **282,** 22102–22111 (2007).
11. Wang, A. *et al.* Nonmuscle myosin II isoform and domain specificity during early mouse development. *Proc. Natl Acad. Sci. USA* **107,** 14645–14650 (2010).
12. Kolega, J. Asymmetric distribution of myosin IIB in migrating endothelial cells is regulated by a rho-dependent kinase and contributes to tail retraction. *Mol. Biol. Cell* **14,** 4745–4757 (2003).
13. Terry, S. J. *et al.* Stimulation of cortical myosin phosphorylation by p114RhoGEF drives cell migration and tumor cell invasion. *PLoS ONE* **7,** e50188 (2012).
14. Amano, M. *et al.* Phosphorylation and activation of myosin by Rho-associated kinase (Rho-kinase). *J. Biol. Chem.* **271,** 20246–20249 (1996).
15. Hu, A., Wang, F. & Sellers, J. R. Mutations in human nonmuscle myosin IIA found in patients with May–Hegglin anomaly and Fechtner syndrome result in impaired enzymatic function. *J. Biol. Chem.* **277,** 46512–46517 (2002).
16. Zhang, Y. *et al.* Mouse models of MYH9-related disease: mutations in nonmuscle myosin II-A. *Blood* **119,** 238–250 (2012).
17. Terasaki, M. *et al.* Stacked endoplasmic reticulum sheets are connected by helicoidal membrane motifs. *Cell* **154,** 285–296 (2013).
18. Billington, N., Wang, A., Mao, J., Adelstein, R. S. & Sellers, J. R. Characterization of three full-length human nonmuscle myosin II paralogs. *J. Biol. Chem.* **288,** 33398–33410 (2013).
19. Surcel, A., Kee, Y. S., Luo, T. & Robinson, D. N. Cytokinesis through biochemical-mechanical feedback loops. *Semin. Cell Dev. Biol.* **21,** 866–873 (2010).
20. Kubow, K. E., Conrad, S. K. & Horwitz, A. R. Matrix microarchitecture and myosin II determine adhesion in 3D matrices. *Curr. Biol.* **17,** 1607–1619 (2013).

METHODS

Mice strains. Knock-in mouse strains expressing GFP–myosin-IIA (GFP–hNMHC-IIA; MHY9$^{\mathrm{GFP}}$) or GFP–myosin-IIB (GFP–hNMHC-IIB) have been previously characterized[10,11], in which the GFP-tagged heavy chains replace the endogenous heavy chain locus, and are expressed under the control of the endogenous promoter. Mice expressing tdTomato–CAAX (Jax Strain 7576; Gt(ROSA)26Sortm4(ACTB–tdTomato,–EGFP)Luo/J) were obtained commercially (Jax Labs) and maintained in the National Heart Lung and Blood Animal Facility. All mouse procedures were performed in accordance with National Heart, Lung, and Blood Institute IACUC guidelines.

Cell culture and imaging. AEC cultures were established and imaged as previously described[4]. Briefly, aortic explants from transgenic donor mice expressing either tdTomato–CAAX (Jax Labs), GFP–myosin-IIA, GFP–myosin-IIB or GFP–myosin-IIA-R709C were cultured in 1.8 mg ml^{-1} collagen in endothelial cell media (EGM2; Lonza). Cells migrating out of the explant were imaged between day 4 and 6 of culture. Drug treatments with blebbistatin (20 µM; Toronto Research Chemicals), cell permeant C3-exoenzyme (100 µg ml^{-1}; Cytoskeleton), Y-27632 (2 µM; Sigma Aldrich) and ML-7 (2 µM, Sigma Aldrich) were performed for 2–12 h before and through imaging periods. Cells were maintained on the microscope stage in an environmental chamber (Pathology Devices) with controlled CO$_2$, humidity and temperature. Cells were imaged using either 20 × 0.75 NA or 60 × 1.20 NA water immersion objective lenses, mounted on a Nikon TE-2000 that was equipped with a Yokogawa CSU X-1 spinning disc, a custom-built laser combiner module (Spectral Applied Research) and a CoolSnap HQ2 CCD (charge-coupled device) camera (Photometrics; pixel size 6.45 µm). Z-stacks were collected using a stage piezo z-stepper (Mad City Labs) integrated onto an XYZ automated stage and controller (Applied Scientific Instrumentation). For imaging using the 60 × 1.20 NA WI objective, each acquired image was binned on camera to improve signal to noise and reduce excitation intensity. The bin size and z-step sizes were matched as closely as possible to achieve near isotropic voxel sizes. Depending on the spatial and temporal resolution required, the voxel size in object space was measured between 215 nm (for 60× at 2 × 2 binning) and 645 nm (20× at 2 × 2 binning). Image acquisition was controlled using MetaMorph Software (Molecular Devices). Full stacks encompassing regions both above and below the cell of interest were collected at intervals of 30 s (for example, for short-term imaging of myosin II dynamics) or 300 s (for example, for long-term imaging of cell migration versus branching over time) seconds to minimize cell photobleaching and photodamage. In panels and videos showing fluorescence images, colour display or contrast has been linearly adjusted for presentation purposes.

Image segmentation. Raw 3D fluorescence images (Supplementary Fig. 1A) were filtered using multiscale Gaussian second partial-derivative kernels (Supplementary Fig. 1B, inset):

$$s(x)_{i,\omega}=\frac{1}{s_{i,\omega}\sqrt{2\pi}}\sum_{\acute{x}}^{\acute{x}\in\Omega_k}\frac{\partial^2 \mathrm{e}^{\frac{-|x-\acute{x}|^2}{2{\sigma_{i,\omega}}^2}}}{\partial {x_i}^2}I(\acute{x})$$

Here σ_i denotes the Gaussian width along dimension i, $\Omega_k=\{\forall\acute{x},|\acute{x}-x_i|\leq 5\sigma_i\}$ denotes the filter kernel support, $I(x)$ is the image intensity at position $x=(x,y,z)$, and $s(x)_i$ is the filter response along the ith dimension, with the maximum of the Euclidean norm across scales defining the filter response magnitude (Supplementary Fig. 1B):

$$S(x)=\max(\{|\mathbf{s}(x)_\omega|\sigma_\omega|\omega=1,\ldots,n\})$$

$$\sigma_\omega=2^{\omega-1}$$

with σ_ω expressed in units of voxels. We refer to the application of this filter as 'surface filtering' because the kernel responds strongly to planar and cylindrical image intensity patterns.

As in a given image volume generally less than 5% is occupied by a cell, a threshold was selected for the filter response distribution as

$$T_{\mathrm{s}}=\overline{S}+3\sigma_{\mathrm{s}}$$

where $\overline{S}$ and σ are robust estimates of the mean and standard deviation of S (ref. 21) effectively treating the cell-occupied voxels as outliers to the background surface-filter response at a 99% confidence level. This thresholding allows segmentation of small, dim branches but can fail in areas with bright, relatively uniform intensities and therefore weak intensity gradients (Supplementary Fig. 1C).

To enhance the segmentation in low-gradient regions we supplemented the surface filtering and thresholding with a two-stage thresholding of the raw image intensities I. First, 'foreground' voxels were selected by thresholding the intensity distribution in the same manner as the threshold for the surface filtering response:

$$T_{\mathrm{f}}=\overline{I}+3\sigma_I$$

Application of the threshold yields a segmentation that selects all voxels above the estimated background, but markedly overshoots the cell membrane owing to out-of-focus light (Supplementary Fig. 1D). A second, more stringent threshold was then selected by Otsu thresholding of these 'foreground' voxels[22] (Supplementary Fig. 1E). The segmented mask is then the union of the voxels that pass either the surface threshold or the high-intensity Otsu threshold (Supplementary Fig. 1F). We refer to the combination of thresholding raw image intensities and surface-filter response as 'surface enhanced' segmentation.

To further improve the robustness of this segmentation and ensure accurate surface reconstruction and topology with a variable and sometimes low image signal to noise ratio, mathematical morphology was used to post-process the mask resulting from the surface-enhanced segmentation. This included area opening to remove small background spots, closure to fill small gaps in the segmented surface, and finally hole filling to ensure that the cytosol, which was not well labelled by the tdTomato–CAAX tag, was included in the segmented cell volume (Supplementary Fig. 1G). These steps were performed using the MATLAB functions bwareaopen, imclose and imfill respectively.

All segmentation was validated as being accurate at the whole-cell level through quantification of membrane label intensity versus distance from the segmented cell surface (Supplementary Fig. 1H), in addition to visual inspection of the segmented cell geometry overlaid on the raw fluorescence intensities using Imaris and the ImarisXT MATLAB interface (Supplementary Fig. 1I).

Skeleton analysis. A binary skeleton image was produced from the cell mask using the iterative thinning algorithm presented in ref. 23. This was implemented as a MATLAB mex-function adaptation of the C code provided in ref. 24. Application of this algorithm converted the cell mask binary image into a binary skeleton image (Fig. 1d). Next, we converted the skeleton image into a graph structure, where branch points are represented by vertices, and are identified in the skeleton image as voxels with more than 2 non-zero voxels in the immediate 26-connected neighbourhood. The branches and cell body are represented by the edges in the graph (Fig. 1g), and are identified as the remaining non-zero skeleton image voxels.

The initial skeleton frequently contained 'false-positive' branch elements, either due to noise in the segmented cell mask or due to features in the cell mask that do not correspond to 'branch-like' structures. We therefore pruned the skeleton to ensure that each branch element had an aspect ratio length to mean radius > 2, and a length > 1 µm.

Skeleton elements, which were proximal to the maximum of the Euclidean distance transform of the cell mask interior and did not meet the above definition of a branch, yet were required to preserve the graph topology, were assigned to the cell body skeleton (Fig. 1g). For the tip–path complexity and length analysis in (Fig. 1h,i and Supplementary Fig. 6A), the shortest path from each branch tip (degree = 1 vertex) in the skeleton graph to the centre of the cell body skeleton was calculated using Dijkstra's algorithm[25] as implemented in the MATLAB function graphshortestpath, with the length of each skeleton element as the edge weight.

Surface curvature analysis. The 3D binary mask image (Supplementary Fig. 2A) was first smoothed by 3D Gaussian filtering with a sigma of 1 voxel, which results in an image volume with values $[0,\ldots,1]$ (Supplementary Fig. 2B). Subsequently, we extracted a triangulated mesh isosurface using the MATLAB isosurface function with an isovalue of 0.5 to preserve volume and surface position (Supplementary Fig. 2C). Note that although this approach to generation of a smooth mesh surface does not strictly guarantee topological consistency with the original mask, alterations in topology were rare, and downstream processing steps did not rely on the mesh surface topology. The smoothed mask was also used to estimate normal vectors to the isosurface using the MATLAB function isnormals (Supplementary Fig. 2D). On the basis of the surface normal we computed for each triangle the Gaussian (K) and mean (H) curvature, applying the numerical method proposed in ref. 26 (Supplementary Fig. 2E).

From the Gaussian and mean curvature we also derived the individual principle component magnitudes, which permitted computation of the maximal absolute local curvature:

$$\kappa_1=H+\sqrt{H^2-K}$$

$$\kappa_2=H-\sqrt{H^2-K}$$

Locally averaged curvatures were then calculated as the mean of all curvatures within a specified sampling radius, r_{s} (Supplementary Fig. 2F).These locally averaged surface curvatures were used when quantifying curvature statistics over entire cells (Fig. 2d–f) or regions of interest (Fig. 6h,i). This ensures that these measures are applied to surface curvature at the same scale as that used when investigating correlations between curvature and intensity, which used a radius of 2 μm to fully sample the adjacent actomyosin cortex (Supplementary Fig. 1H).

For assignment of surface regions into the geometric classes illustrated in Fig. 2a,b, and Supplementary Fig. 3C,D, thresholds on the mean ($0\,\mu\mathrm{m}^{-1}$) and Gaussian ($\pm 0.1\,\mu\mathrm{m}^{-2}$) curvature were used, where for Gaussian curvature this small non-zero value accounts for measurement noise. To quantify the relative amount of each class present in cells from a given condition, the number of surface mesh triangles that fit the threshold for each category was counted (Supplementary Fig. 3A,B).

Correlation between surface curvature and image intensity. To limit the analysis to subcellular localization variation, intracellular image intensities were normalized before correlation analysis by setting the standard deviation equal to 1 and setting the whole-cell means to be equal, with the minimum value across all data sets set to zero. For correlations between surface curvature and subcellular fluorescence intensity, samples were produced for each voxel on the surface of the cell mask. The intensity value in a surface voxel was determined by the average of image intensities within the volume intersection of the cell mask with a sampling sphere of radius r_s centred on the voxel. Similarly, the curvature value in a surface voxel was determined by the average of the curvature of every triangulated surface mesh face falling within this sampling sphere. Importantly, in 3D data sets the sampling geometry is inherently coupled to the local cell-surface geometry, which leads to apparent correlations between intensity and curvature. This artefact is illustrated with a synthetic image that is constructed with a real cell geometry but the intracellular image intensities vary only with distance from the cell surface (Supplementary Fig. 4A):

$$I_s(x) = A\mathrm{e}^{-\frac{D(x)^2}{\sigma_c{}^2}} + \varepsilon(x)$$

Here, I_s denotes the simulated image, with a uniform cortical intensity band of amplitude A and width σ_c, $\mathrm{D}(x)$ is the Euclidean distance from any location x inside the cell to the closest point at the cell surface, and ε is normal I.I.D. noise. Although the intensity does not vary along the cell surface, or correlate with curvature, it shows a statistically significant correlation with curvature (Supplementary Fig. 4B, blue), due to the effective mean sample depth varying systematically with curvature (Supplementary Fig. 4C).

To correct for this bias, we can decouple variation in fluorescence intensity along the cell surface from the systematic variation with depth into the cell (Supplementary Figs 1h and 4D) by computing a 'depth-normalized image' $I_N(x) = \frac{I(x)}{B(\mathrm{D}(x))}$ (Supplementary Fig. 4E), where

$$B(d) = \frac{1}{N_D}\sum_{x}^{x\in\Omega_d} I(x)$$

is the normalization constant for depth d (in voxels), with

$$\Omega_d = \{x \mid d-1 < D(x) \le d\}$$

denoting the set of all pixels at depth d and N_D the number of voxels in this set. This depth-normalized image has equal mean intensities at each distance from the cell surface, while preserving any variation in intensities along the cell surface (Supplementary Fig. 4E). Accordingly, the correlation artefact due to variation in the sample penetration depth is removed (Supplementary Fig. 4B, red), except for at the highest and lowest intensities. This remaining artefact is due to variation in sample size with curvature (Supplementary Fig. 4F), and the same artefact is seen in a simulated image that contains only I.I.D. noise (Supplementary Fig. 4G,H). This is because the smallest samples occur in the highest-curvature areas, and extreme values in random data are more probable in smaller samples, leading to a correlation between sample intensity and sample size (Supplementary Fig. 4I). However, these artefacts are diminished for a signal that is spatially autocorrelated (Supplementary Fig. 4J) such as

$$I_s(x) = A\beta(x, s_{\mathrm{AC}}) + B\varepsilon(x)$$

Here β represents an I.I.D. random variable filtered with a Gaussian of size σ_{AC} to spatially correlate the values. The final image signal is given by multiplying β with magnitude A and superposition of a spatially uncorrelated I.I.D. noise ε with amplitude B. The correlation between neighbouring image values decreases the dependence of a given sample value on the sample size, limiting this artefact to the upper and lower 10% of image intensities in data with a relatively low signal to noise ratio (Supplementary Fig. 4K,L). With experimental fluorescence images the minimal length scale of the spatial autocorrelation is defined by the spatial extent of the microscope's point-spread function (PSF). Correlations over longer distances are often observed owing to the micrometre length scales of chemical signals that control the spatial variation in molecular localization within a cell. Indeed, on our experimental data we observed minimal shifts of the intensity versus curvature curves after applying depth normalization (Supplementary Fig. 4M), in contrast to the shift seen in correlations due purely to artefacts (Supplementary Fig. 4B), suggesting that the correlations we found between these two variables are unlikely due to depth-variation artefacts.

We also tested the effect of PSF geometry on correlations between curvature and fluorescence intensity. A spatially autocorrelated simulated image I_s (Supplementary Fig. 4J) was convolved with a simulated PSF image that approximates the geometry of the PSF observed in experimental images (Supplementary Fig. 2J). This produced correlation artefacts different from those in raw images (Supplementary Fig. 2K), but still limited to extreme intensity values. The different trends at high and low intensities were due to the orientation of the cell geometry used in these simulations relative to the imaging axis, which was confirmed by performing the same simulations with an artificial geometry that had no preferential orientation relative to the imaging axis (Supplementary Fig. 2L). In this case only very small correlation artefacts were observed, well below the variations in curvature measured experimentally (Supplementary Fig. 2M), indicating that this effect was not the source of the correlations we observed. This is further supported by the lack of correlation between intensity and curvature in images of uniformly fluorescent microspheres (Supplementary Fig. 2H) and between a membrane label and curvature (Supplementary Fig. 5A,B). Therefore, we conclude that our segmentation and fluorescence measurements accurately reflected real spatial distributions of fluorophores and their correlation with respect to curvature in 3D images.

For the correlations between curvature and image intensity in subcellular regions of interest in Fig. 6h,i, small rectangular regions were manually selected, and the mean surface curvature and cortical intensity over the entire region of interest was used for quantification. These fluorescence intensities were first photobleach-corrected through a double-exponential fit before correlation with curvature.

Co-localization analysis. For 2D histograms measuring co-localization of myosin II and F-actin in untreated and blebbistatin-treated cells (Fig. 5l,m), images were first background subtracted. Then 2D histograms were constructed by pooling intensity data across multiple cells, using only the image voxels from each cell that were within the segmented cell boundary and within the cortex (distance from segmented cell membrane less than or equal to the sampling radius $r_s = 2\,\mu\mathrm{m}$).

Cell migration analysis. To quantify motion of the cell body, a standard centroid calculation was ruled out, as the location of the centroid depends on all voxels in the mask, including those in the branches. This would therefore introduce an inherent correlation between the cell body motion and number and structure of the branches. Instead we found the maximum value of the Euclidean distance transformation of the mask interior (Supplementary Fig. 7A,B), which roughly corresponds to the centre of the subcellular region of maximum radius, and its location differs significantly from that of the centroid (Supplementary Fig. 7C).

Fluorescence recovery after photobleaching (FRAP) analysis. AECs derived from MHY9$^{\mathrm{GFP}}$ mice were cultured as described above. Cells were imaged using the spinning disc confocal microscope system described above. The microscope system was equipped with a digital micro-mirror device (DMD; Mosaic, Andor Technology) to guide 488-nm laser illumination (Sapphire HP, Coherent) through a separate illumination port to the specimen plane. Laser light was defocused to illuminate the entire DMD. Total power delivered to the DMD area was ~100 mW. Activation of specific micro-mirrors within the DMD steered illumination to the specimen within user-defined regions of interest. Switching between photobleaching illumination and imaging excitation illumination was accomplished through motorized port switching controlled by Metamorph software. Target regions for photobleaching were selected in Metamorph using custom-drawn regions of interest traced onto spinning disc confocal images, which were then used to create masks for application of photobleaching illumination. Cell branches that were perpendicular to the imaging axis (parallel to the *XY* plane) were chosen for analysis for consistency between samples. Three pre-bleach images were acquired before bleaching for each field of view. Target regions were bleached with one 300 ms bleach pulse and recovery was imaged every 1 s for 10 s and then every 3 s for the next 45 s. Intensities of the bleached region; an adjacent, unbleached region on the cortex; and image background were extracted from the images and imported to Microsoft Excel. After background subtraction, fluorescence recovery was normalized first to the average pre-bleached signal and then to image photobleaching of the unbleached cortical region[27]. To calculate the percentage of recovery, single and double exponentials were fitted to the resulting data as described previously[4,28] . In our experience,

DOI: 10.1038/ncb3092

single-exponential fits often overestimate the total recovery, consistent with multiple interactions in the pool of fluorescent molecules[29]. Reported here are the data for double exponentials, although the same trend was observed for single-exponential fits. Curves that deviated from both single- and double-exponential fits were discarded. Local branch diameters were measured from pre-bleach images. P values of the difference in myosin II turnover between large and small branches were derived from Student's two-tailed t-test.

Agarose chamber fabrication, cell culture and imaging. Template moulds were microfabricated using photolithography of SU-8 on silicon wafers. The dimensions of each chamber were 30 μm depth, central chamber diameter of 20 μm and 'branches' with 5 μm width and 20 μm length. These dimensions were chosen to allow cells to spread completely with no overlap between the branches. The template moulds were used to produce poly(dimethylsiloxane) (PDMS; Sylgard 184; Dow Corning) stamps. The stamps were placed onto acid-washed, poly-L-lysine-coated glass-bottomed MatTek dishes (MatTek). A molten 0.6% agarose solution in 30% ethanol was then wicked around the stamps, and allowed to cool. The stamps were removed and the resulting agarose chambers were rinsed in phosphate buffered saline (PBS). A 100 μg ml^{-1} collagen solution was used to coat the poly-L-lysine surface, followed by extensive rinsing in PBS. Human umbilical vein cells (HUVECs; Lonza) were transfected by electroporation with constructs expressing GFP–myosin-IIA and mcherry–CAAX and allowed to adhere to plastic culture dishes for 4–6 h. Transfected HUVECs were trypsinized and allowed to spread into the agarose chambers in endothelial medium (EGM2, Lonza) for approximately 60–90 min before imaging live. Cells were imaged using similar imaging parameters as above. Cells that did not completely fill the lateral area of the chamber were discarded for analysis to ensure that the lateral cell shape was confined by the agarose chamber.

To show mean cortical CAAX and GFP–myosin-IIA as well as the normalized ratio of myosin IIA/CAAX within the chambers, cells were segmented and processed as described for cells in collagen gels, with local surface curvature and GFP–myosin-IIA intensity mapped to the surface of each cell, and used to determine a curvature, CAAX and myosin IIA intensity value at each voxel position. Regions of interest in the axial dimension where the cells were confined by the agarose chamber of multiple cells were selected, aligned in z, and a Gaussian filter applied to smooth the distribution laterally. These voxel data were then used to determine a mean value at each X, Y position for curvature, CAAX and myosin II intensity, which was mapped using the colour scales shown. CAAX reporter and GFP–myosin-II signals were normalized to individual maximum intensity before computing the ratio.

Statistical methods. Histogram error bars showing 1.96∗standard error of the mean (s.e.m.) in Fig. 1h,i were generated treating each cell as a single data point, that is, using the standard deviation of the values in each bin across cells, with n being the number of cells. The curvature category data in Fig. 2d failed an Anderson–Darling test of normality and therefore P values were calculated using a Wilcoxon rank sum test. Data in Fig. 2e passed an Anderson–Darling normality test and P values were calculated using Welch's two-tailed t-test with unequal variances. All Spearman's correlation values (ρ) were confirmed as non-random by calculating P values using the exact permutation distribution. For Figs 3g–j, 4h and 5d–f,h,j, individual samples from a single cell can overlap with other adjacent surface samples from that cell. To determine the confidence intervals in this case 1,000 repetitions of a subsampled bootstrap were computed. The number of samples in each bootstrap was chosen such that the samples were completely non-overlapping (total sample area less than total cell-surface area). Confidence intervals for cross-correlation curves in Fig. 6c,e,i were calculated using 1,000 bootstrap repeats of a variance-stabilized transformation of the individual (per-cell) cross-correlation curves. The confidence intervals of the linear relationship in Fig. 6f were estimated using a numerical approximation of the solution's Jacobian using the MATLAB function confint.

Software availability. Software is available on request from the Danuser laboratory. It is command-line driven MATLAB code and therefore requires some knowledge of MATLAB syntax to operate. The software requires Imaris version 7.4 or earlier with the ImarisXT module for visualization of analysis results overlaid on images.

Repeatability of experiments. All imaging experiments were performed on at least three separate culture preparations (each from a single mouse), imaged over two or more imaging sessions. Data for any given condition (drug concentration, mutant and so on) were then pooled. For FRAP analysis, two independent cell culture preparations and imaging sessions were performed, and the data pooled. For live-cell imaging, data shown are representative of four independent cultures used for at least 6 imaging sessions.

Sample sizes determination, randomization and blinding. No statistical method was used to predetermine sample size. The experiments were not randomized, and the investigators were not blinded to allocation during experiments.

21. Rousseeuw, P. J. & Leroy, A. M. *Robust Regression and Outlier Detection* (John Wiley, 1987).
22. Otsu, N. Threshold selection method from gray-level histograms. *IEEE Trans. Syst. Man Cybern.* **9,** 62–66 (1979).
23. Palagyi, K., Kuba, A. in *Combinatorial Image Analysis: 14th International Workshop, IWCIA 2011, Madrid, Spain, May 23–25, 2011. Proceedings* Vol. 61 (eds Aggarwal, J. K. *et al.*) 199 (Springer, 1999).
24. Cornea, N. D., Silver, D. & Min, P. Curve-skeleton properties, applications, and algorithms. *IEEE Trans. Vis. Comput. Graph* **13,** 530–548 (2007).
25. Dijkstra, E. W. A note on two problems in connexion with graphs. *Numerische Mathematik* **1,** 269–271 (1959).
26. Theisel, H., Rossi, C., Zayer, R. & Seidel, H-P. *Proceedings of the 12th Pacific Congress on Computer Graphics and Applications, Seoul, Korea, 6–8 October, 2004* 288–297 (2004).
27. Phair, R. D., Gorski, S. A. & Misteli, T. Measurement of dynamic protein binding to chromatin *in vivo*, using photobleaching microscopy. *Methods Enzymol.* **375,** 393–414 (2004).
28. Pasapera, A. M., Schneider, I. C., Rericha, E., Schlaepfer, D. D. & Waterman, C. M. Myosin II activity regulates vinculin recruitment to focal adhesions through FAK-mediated paxillin phosphorylation. *J. Cell Biol.* **188,** 877–890 (2010).
29. Klein, C. & Waharte, F. in *Microscopy: Science, Technology, Application, and Education* (eds Mendez-Vilas, A. & Diaz, J.) 772–783 (Formatex Research Center, 2010).
30. Dasanayake, N. L. & Carlsson, A. E. Stress generation by myosin minifilaments in actin bundles. *Phys. Biol.* **10,** 036006 (2013).
31. Verkhovsky, A. B., Svitkina, T. M. & Borisy, G. G. Myosin II filament assemblies in the active lamella of fibroblasts: their morphogenesis and role in the formation of actin filament bundles. *J. Cell Biol.* **131,** 989–1002 (1995).

DOI: 10.1038/ncb3092

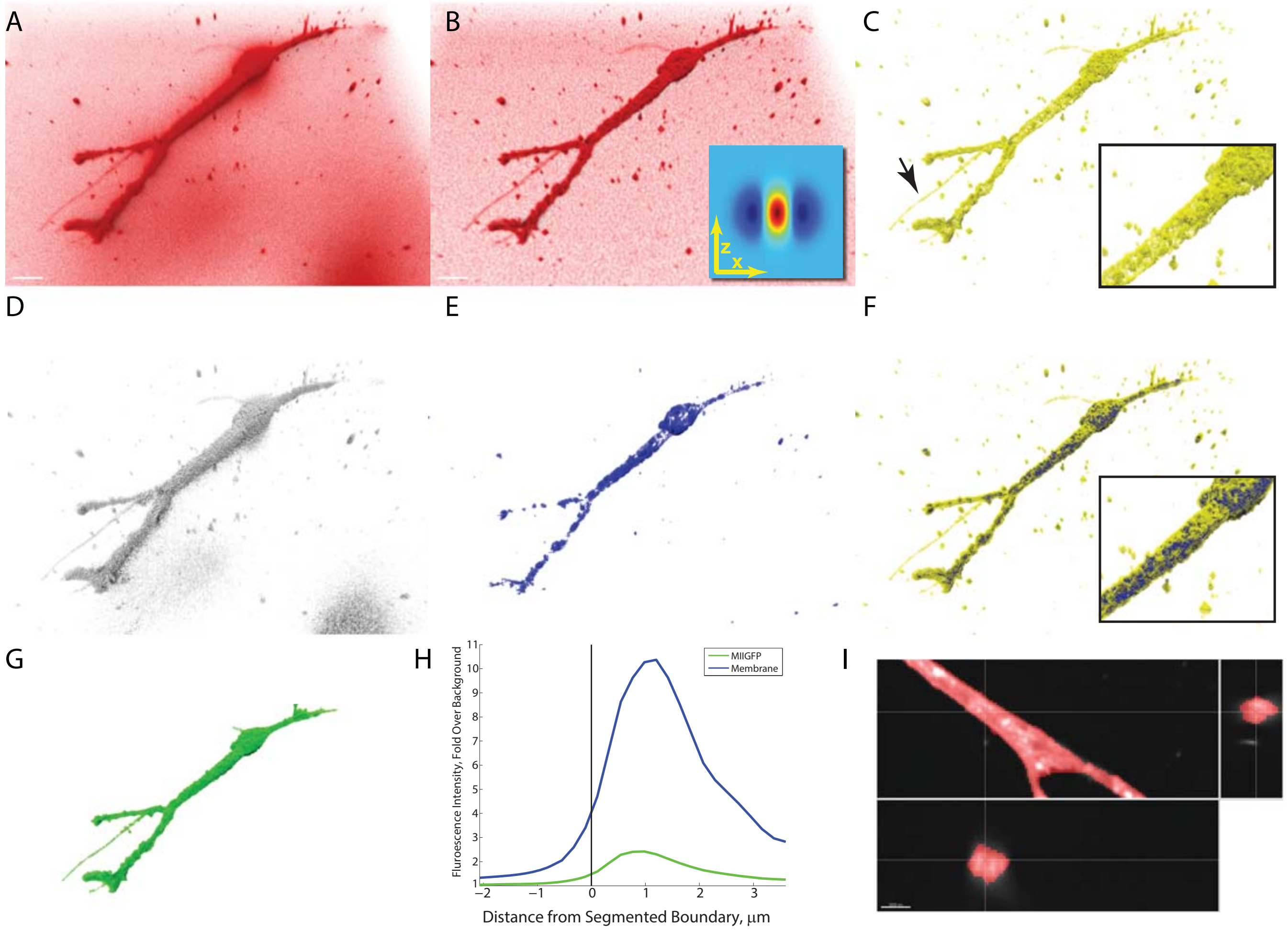

Supplemental Figure 1 Surface enhanced segmentation of membrane-labeled cells. (A) Raw membrane label fluorescence image and (B) Surface filtered image showing a cross-section of one filter kernel as inset. Bar equals 10 μm. (C) Thresholded surface filter response. The surface filter enhances the weak contrast of small dim features (arrow). Inset: variations in the surface labeling leads to holes in the segmented filter response (D-E) Two–stage intensity thresholding first determines foreground voxels (D), and then a high-intensity population within the foreground (E). (F) The union of the thresholded surface filter response and thresholded intensity image gives the initial segmentation of the cell volume. Inset: intensity thresholding provides complementary information to the surface filtering. (G) Morphological post-processing of the initial segmentation to remove features in the background and improve robustness of the cell surface representation. (H) A plot of fold-intensity over background as a function of distance from the segmented cell surface. Green line is for myosin IIB-GFP, blue line is for membrane stain (see methods). Negative numbers indicate region outside of the segmented volume of the cell. (I) Visual inspection of the raw image fluorescence (gray) with the segmentation (red) superimposed allow validation of the segmentation. XY, XZ, and YZ panels are shown to illustrate all views.

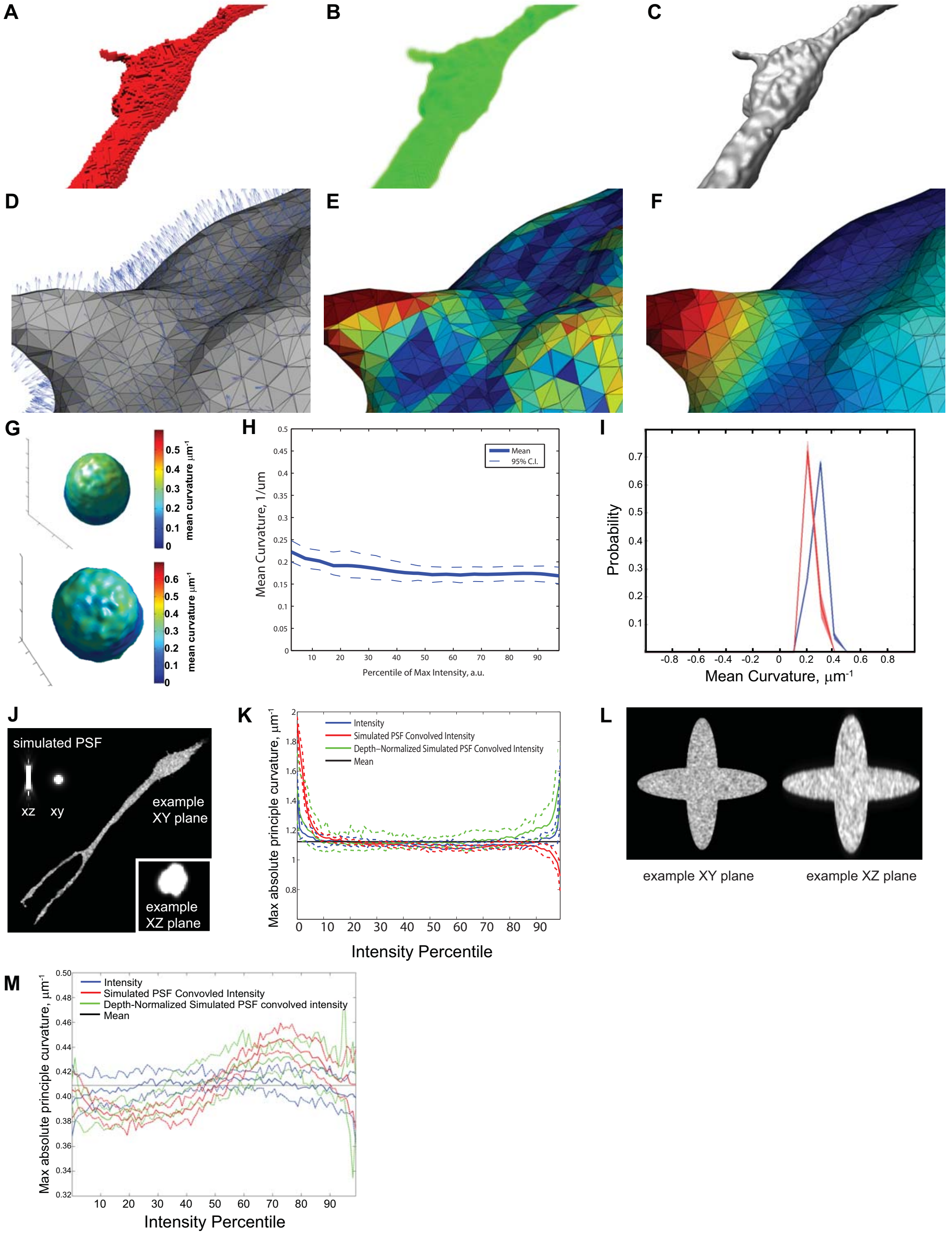

Supplemental Figure 2 Determination of local curvature at the cell surface. (A - F) The segmented voxels representing the cell surface (A) are first smoothed (B) and then an isosurface is determined (C), along with the normal vectors to the surface(D). The surface curvature at each isosurface mesh face is calculated (E) followed by local averaging (F). (G) Surface segmentation and mean curvature validation of imaged microspheres. Fluorescent microspheres of 6 µm (top) and 10 µm (bottom) diameter beads were imaged and segmented as described for cells, and local mean surface curvature was deteremined. (H) Distributions of intensity percentiles as a function of curvature on bead samples. Solid line equals mean value, dashed line indicates 95% confidence limits about the mean from n=3 beads.. (I) Probability distributions of measured local curvature for 10 µm (red) and 6 µm (blue) beads. Note that the dertermined peaks correspond tightly to the known radii of curvature of imaged beads. Solid lines indicate mean from n=3 beads each, with shaded area around lines indicating +/- 1.96 SEM. (J) Simulated z-stretched PSFs (inset) were convolved with a simluated test image to test for potential artifacts in segmentation on imaging geometry. (K) shows correlation of depth-normalized intensity vs maximal absolute principle curvature. In the central 90 percentile of intensity ranges, the correlation is flat, indicating that no bias is derived from an extended z-stretch on segemted. (L) Even with a simulated test image of known geometry and simulated z-stretched PSF, only a slight bias is introduced (red lines), with a slight positive slope when compared with the simulated intensity (blue lines). When this is corrected by depth-normalization, the bias is reduced (green lines). In H,K and M dashed lines indicate boot-strapped 95% confidence intervals and in K and M solid lines indicate means from n=10 simulations each.

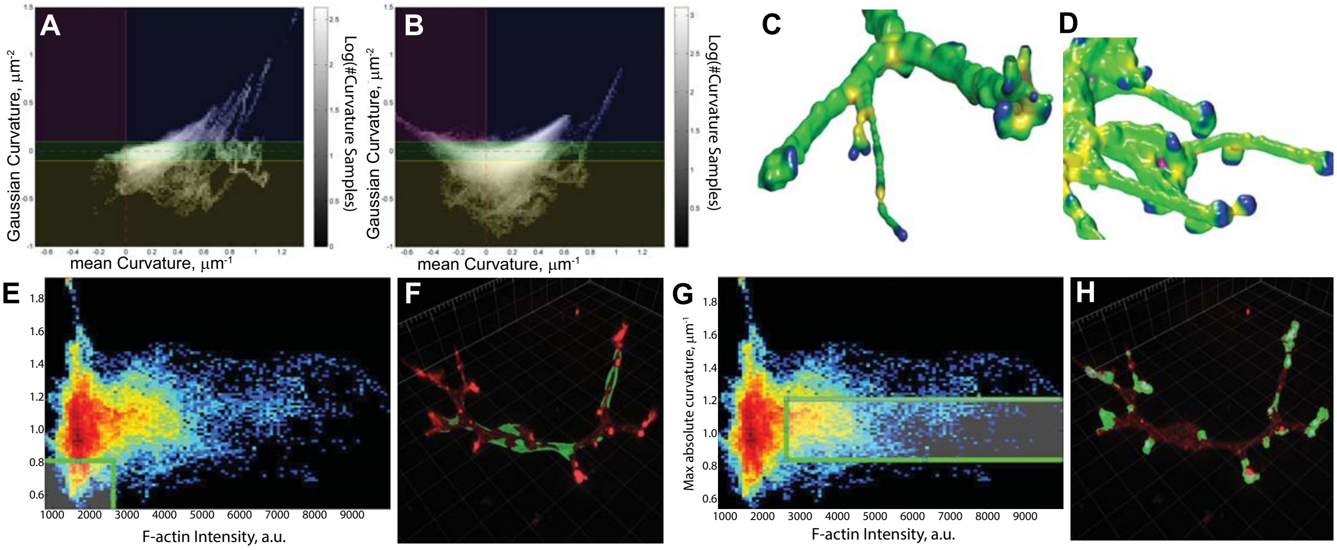

Supplemental Figure 3 (A,B) Surface points in control (A) and blebbistatin (B) treated cells can be classified into different categories (colored highlights) by thresholding the Mean and Gaussian curvature. (C,D). This permits comparison of the fraction of surface mesh triangles in each category between experimental conditions (see Figure 1). (E-H) Local surface curvature vs. F-actin at the cortex. (E) 2D histogram of maximum absolute curvature vs F-actin intensity via phalloidin stain for an example cell (shown in F). The colors represent $\log_{10}$ of the surface points counted, as in Figure 3. Green box indicates region of voxels selected with a given range of curvature and F-actin intensity. These are then mapped back to the cell surface (F, green). Similarly, a higher range of F-actin intensities at a higher range of curvature values (G) can be mapped onto the surface (H, green), highlighting predominantly tip structures.

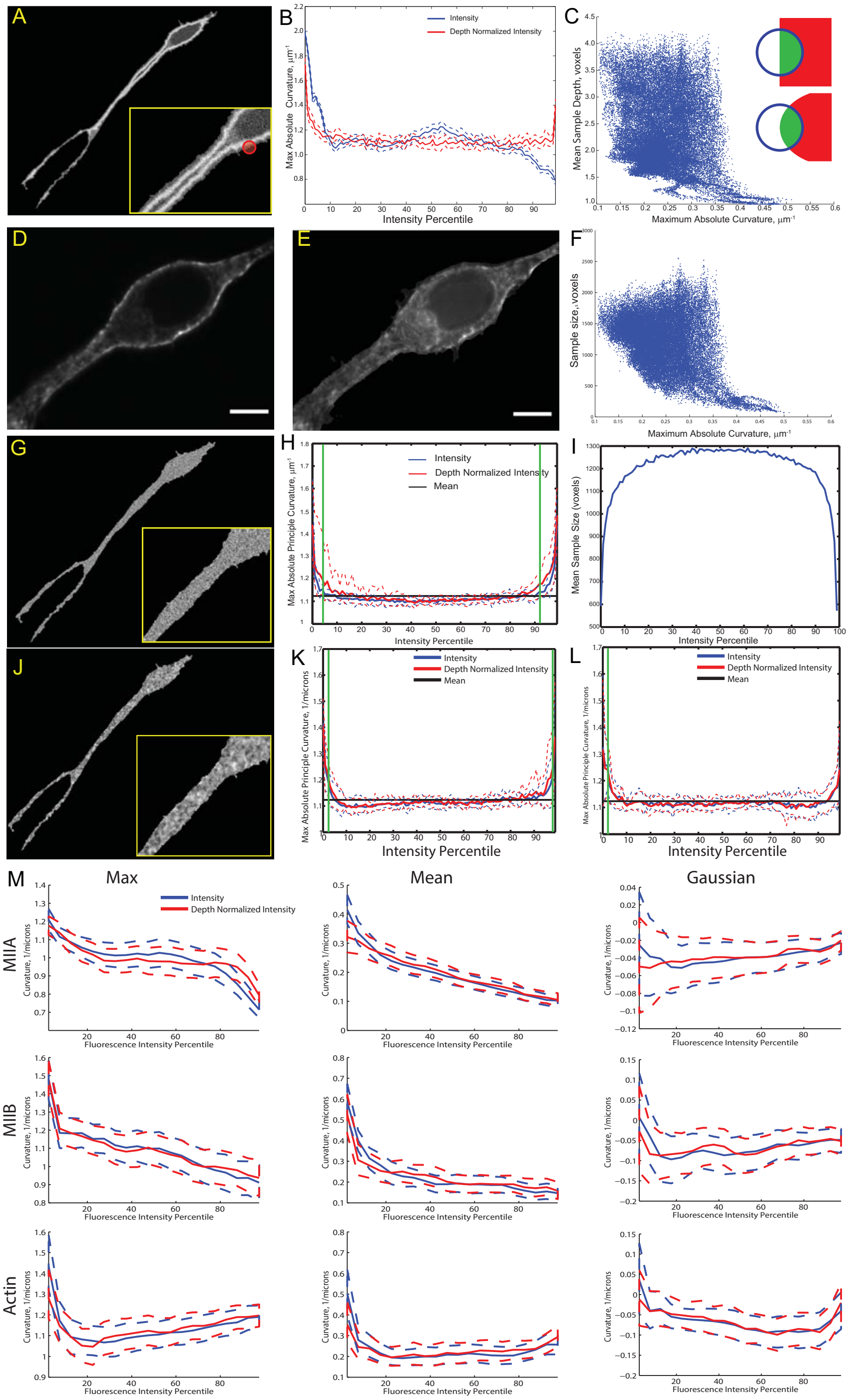

Supplemental Figure 4 Artifacts in surface intensity sampling due to cell geometry and depth-dependent fluorescence variation. (A) A simulated cell image in which intensity varies only with the distance from the cell surface but is uniform along the surface shows correlation between curvature and intensity (B, blue). Inset, red: Illustration of sampling sphere. (C) The correlation is due to variation in effective sample depth with curvature. Inset: cartoon to illustrate that the effective mean sample depth varies with curvature. Cell is shown in red, sampling sphere in blue. Different cell curvatures give different sample geometries (green, compare top and bottom) n=10 simulations. (D) Similar depth variation is seen in experimental data. (E) Depth normalization (see Supplementary Information 'Curvature and Image Intensity Correlation') removes systematic intensity variation with depth in experimental images, but when applied to simulated image some artifact remains (B, red) due to variation in sample size with curvature. n=10 simulations. (F). (G) An image with only noise shows the same correlation between intensity and curvature (H), and a correlation between intensity and sample size (I). A random signal with spatial autocorrelation of $\sigma_{AC}=1$ (J) shows diminished artifactual correlation (K), which decreases further with $\sigma_{AC}=2$ (L). Green vertical lines in (H, K, L) indicate the percentile levels of image intensities below/above which the surface curvature and intensity display a significant correlation, i.e. the curvature values for a small range of particular intensity values deviate significantly from the mean surface curvature value over the entire cell. (M) Applying depth normalization to the experimental data only alters the observed correlations at very low intensities, i.e., below the 10th percentile. In B,H,I,K,L and M dashed lines indicate boot-strapped 95% confidence intervals and solid lines indicate means from n=10 simulations each.

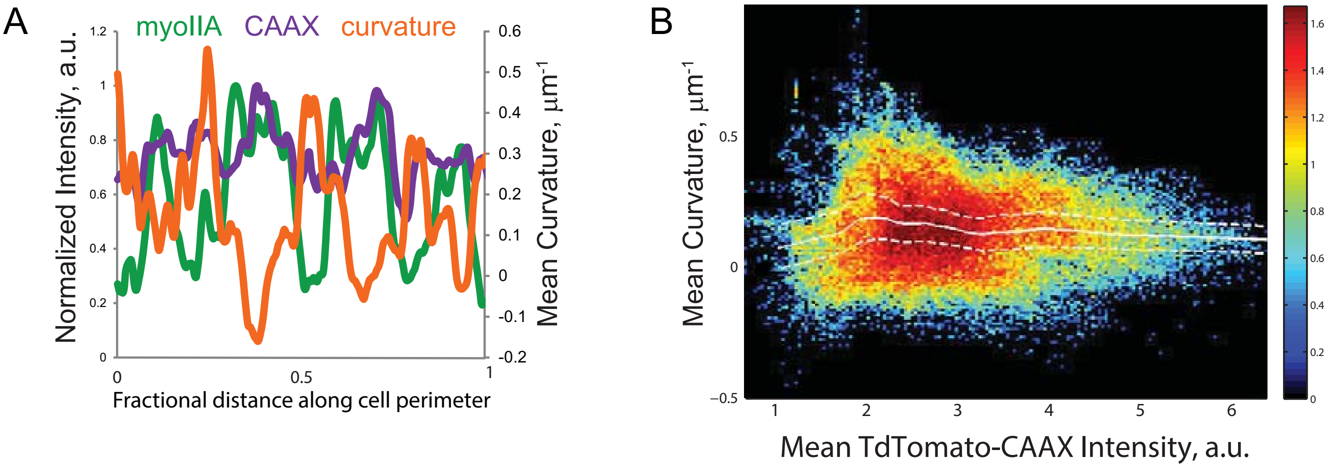

Supplemental Figure 5 Membrane localized Td-Tomato-CAAX does not show curvature dependence in cells confined in agarose chambers. Endothelial cells confined in agarose coffins were imaged and registered to obtain average positional intensity, as described in main text and Methods. (A) Normalized mean intensity of GFP-myosin IIA (green), Td-Tomato-CAAX (purple) and calculated mean curvature as a function of distance along the confined borders of cells as shown in Figure 4. CAAX signal shows some fluctuations, but are not correlated with curvature. (B) Probability distribution of mean curvature versus mean Td-Tomato-CAAX for all points along confined cell boundaries. n= 6 cells, 95126 points. Spearman's ρ= -0.093, p=8.8 x 10^{-164}. Solid white line indicates mean and dashed lines indicate bootstrapped 95% confidence intervals.

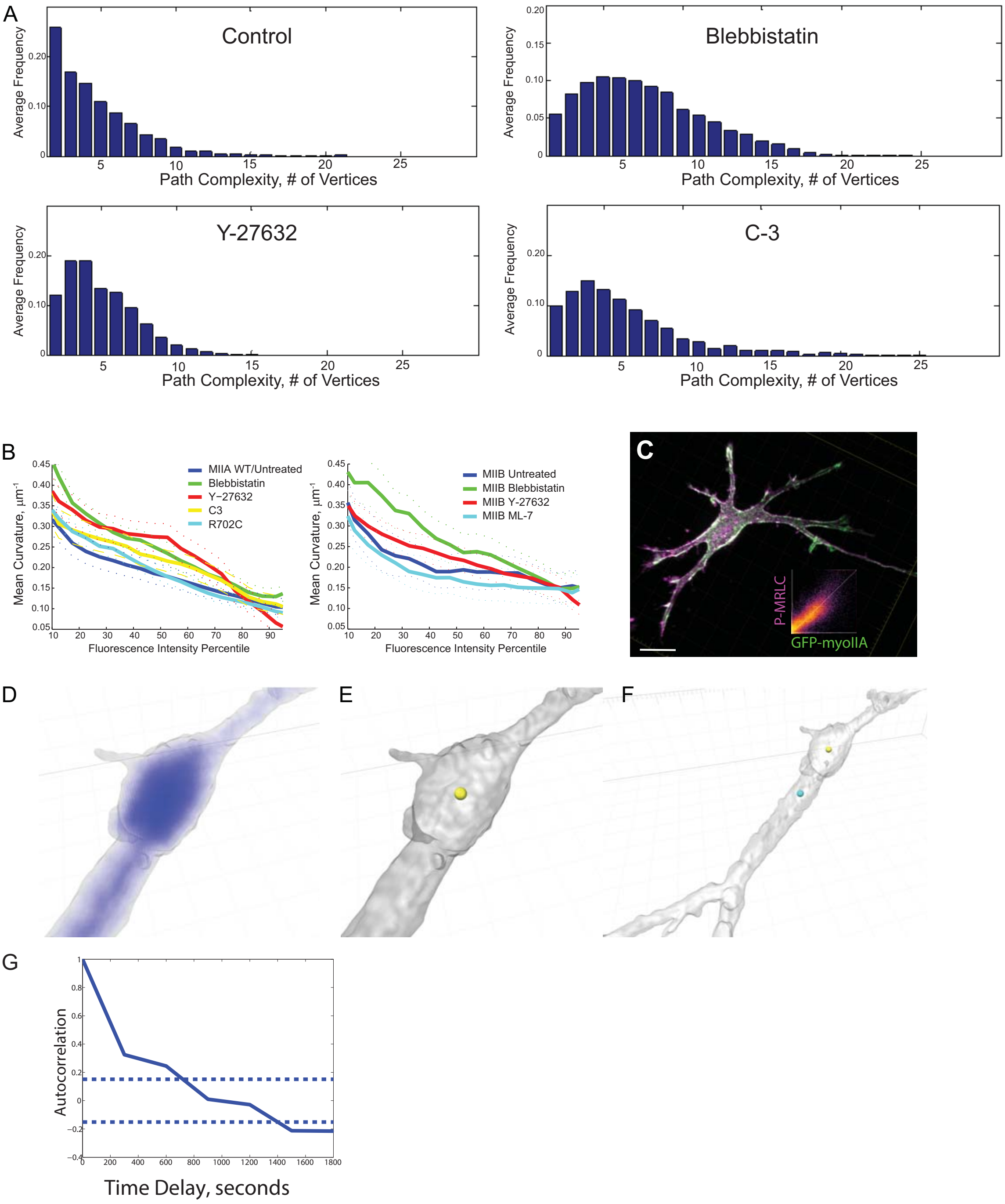

Supplemental Figure 6 Inhibition of rho-ROCK or myosin II activity increases cell branch complexity but has no effect on myosin II localization to the cortex. (A) Cells were treated with blebbistatin, Y-27632, or C-3 and branch path complexity determined as described in Figure 1. Note control and blebbistatin data is re-plotted from Figure 1 here for comparison. (B) Comparison of drug treatments or mutations (R702C) on cortical localization of myosin IIA (left) compared to myosin IIB (right). Plot shows mean curvature as a function of myosin IIA or IIB intensity percentile. Solid lines indicate mean and dashed lines indicate bootstrapped 95% confidence intervals.(C) An AEC expressing myosin IIA-GFP (green) in a 3D collagen gel was fixed and phospho-serine-19 myosin II regulatory light chain was immunolocalized (purple). Maximal intensity projection of a 3D reconstruction, inset: Co-localization plot of fluorescence intensities. Bar equals 10 μm. (D-F) Computation of a cell center reference that is robust against cell morphological variations. (D) The Euclidean distance transform (blue) measures distance from the cell surface (grey). (E) The maximum of the distance transform (yellow) defines the centermost point in the cell volume (F), which deviates significantly from the actual centroid (blue). (G) Autocorrelation of cell center speed over time (blue line). Dashed line shows 99% confidence bounds. N= 8 cells for 240 time points.

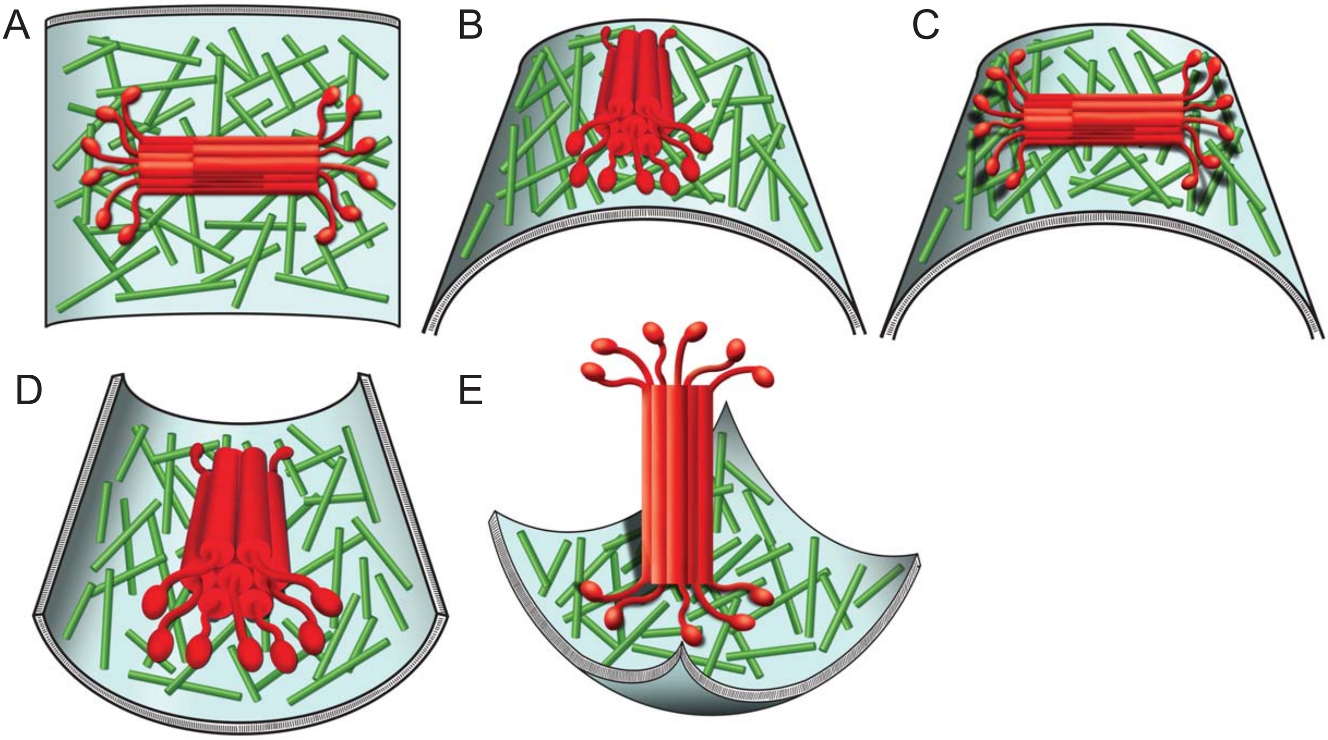

Supplemental Figure7 Model of myosin II mini-filament assembly onto cortical actin patches of different curvature. Myosin II mini-filaments form stiff 300 nm rods, with bouquets of heads that extend an additional 40-50 nm on either side of the rod, giving a total length of nearly 400 nm[13]. Given an isotropic meshwork of actin filaments (green) at the cortex, the maximal engagement of heads at each end may occur in regions of minimal curvature (A). For simplicity, consider alteration of curvature along a single axis. As the cortex and membrane curve concavely (B), the optimal orientation of the myosin minifilament for full head engagement is along the axis of least curvature. Intriguingly, in a pseudopodial extension this axis corresponds to the longitudinal axis and aligns myosin minifilaments with the direction pseudopod retraction. If the curvature of the cortex is convex (C), optimal head engagement will fail only as the curvature becomes higher than will allow both head bouquets to access the cortex equally. Here again, myosin minifilament orientation along the axis of lowest curvature allows maximal head engagement (D). Consistent with this, recent simulation data support the notion that myosin-II minifilaments can rotate in the cortex to maximally engage and generate stress[30]. Such limitations on a > 300 nm filament would effectively prevent maximal engagement of heads in a tip structure of similar size (E). In the cell, these examples may be multiplied over larger curvature scales as groups of myosin II minifilaments assemble on to the cortex in larger macromolecular assemblies[31].

Supplemental Video Legends

Supplemental Video 1 Morphology of AEC migrating in a 3D collagen gel. 3D z-stacks of AECs expressing TdTm-CAAX were acquired at 10 minute intervals using a spinning disk confocal microscope. Shown is maximum intensity projection reconstruction. Grid scale: Major tick marks, 10 μm. Total elapsed time shown at lower right in min.

Supplemental Video 2 Thinning-based skeletonization of AEC surface to determine morphological skeleton. First frame: rendering of the segmented surface. Subsequent frames show successive rounds of computational thinning to achieve the morphological skeleton. Frame size is 130 μm lateral x 65 μm axial.

Supplemental Video 3 Curvature category mapping on the surface of a control cell. Segmented surface of a control cell colorized with curvature categories as described in Figure 1 and Supplemental Figure 2. Rotation is around the z-axis of imaging. Total frame size is 100 μm x 63 μm.

Supplemental Video 4 Curvature category mapping on the surface of a cell treated with 20 μM blebbistatin, with curvature categories as described in Figure 1 and Supplemental Figure 2. Rotation is about an axis 70 degrees off of the z-axis, to show sides of thin branches. Total frame size is 95 μm x 60 μm.

Supplemental Video 5 3D Branch tracking of an AEC migrating in 3D collagen gel. Maximum intensity reconstruction of fluorescence (red) of an AEC expressing TdTm-CAAX migrating in a 3D collagen gel. Time-lapse 3D image sequence was collected by spinning disk confocal microscopy at 10 minute intervals (elapsed time shown in lower right as hours:min:sec). In each frame, the position of the cell morphological skeleton is shown in green (branches) and blue (body segments), and branch tips and vertices are highlighted with large and small red spheres, respectively. Morphological skeleton evolution over time is shown in color scale from purple (T =0) to white (T= 300 min) show in white. Scale grid = 5 μm, minor tick marks = 1 μm. Total elapsed time shown at lower right in minutes.

Supplemental Video 6 Centroid tracking of an AEC migrating in 3D collagen gel. Maximum intensity reconstruction of fluorescence (red) of an AEC expressing TdTm-CAAX migrating in a 3D collagen gel collected by 3Dspinning disk confocal microscopy imaging at 10 minute intervals. The blue sphere shows the centermost point, the colored trace shows path over time, with red indicating the starting frame and white indicating final position. Grid scale = major tick marks, 5 μm, minor tick marks = 1 μm. Total elapsed time shown at lower right in minutes.

Supplemental Video 7 Maximal curvature mapped to surface of a control cell during migration and shape change. Red values indicate highest maximal local curvature, blue values indicate lowest values. Scale grid is in microns. Time interval between frames is 300 seconds.

Supplemental Video 8 Example of a segmented region of interest fused for analysis of local curvature and cortical GFP-myosin IIA intensity over time. Maximum intensity reconstruction of fluorescence (red) of time-lapse 3D imaging of an AEC expressing GFP-myosin-IIA collected by spinning disk confocal microscopy at 10 minute intervals during migration in a 3D collagen gel . Grey area indicates region segmented and cropped for surface curvature measurement and cortical GFP-myosin-IIA intensity. Time stamp shown in lower left in min, total time 60 minutes. Grid spacing = 10μm.

Supplemental Video 9 Myosin IIA accumulation at normal and non-normal branch bases. Maximum intensity reconstruction of fluorescence (red) of time-lapse 3D imaging of an AEC expressing GFP-myosin-IIA collected by spinning disk confocal microscopy at 3 minute intervals during migration in a 3D collagen gel. Frame playback is paused during movie presentation to illustrate regions of cortical GFP-myosin IIA accumulation at the base of branches oriented normal or non-normal to the major axis of the cell body. Grid spacing = 10 μm. Total elapsed time shown at lower left in min.